



**Calhoun: The NPS Institutional Archive**  
**DSpace Repository**

---

Faculty and Researchers

Faculty and Researchers' Publications

---

2008

A conservative discontinuous Galerkin  
semi-implicit formulation for the  
Navier-Stokes equations in nonhydrostatic  
mesoscale modeling

Restelli, Marco; Giraldo, Francis X.

---

M. Restelli, F.X. Giraldo "A Conservative Discontinuous Galerkin Semi-Implicit Formulation for the NavierStokes Equations in Nonhydrostatic Mesoscale Modeling" SIAM Journal of Scientific Computing, v. 31,#3, (May 7, 2009), 22312257. (27 pages)  
<http://hdl.handle.net/10945/55894>

---

This publication is a work of the U.S. Government as defined in Title 17, United States Code, Section 101. Copyright protection is not available for this work in the United States.

*Downloaded from NPS Archive: Calhoun*



Calhoun is the Naval Postgraduate School's public access digital repository for research materials and institutional publications created by the NPS community. Calhoun is named for Professor of Mathematics Guy K. Calhoun, NPS's first appointed -- and published -- scholarly author.

**Dudley Knox Library / Naval Postgraduate School**  
**411 Dyer Road / 1 University Circle**  
**Monterey, California USA 93943**

<http://www.nps.edu/library>

# A CONSERVATIVE DISCONTINUOUS GALERKIN SEMI-IMPLICIT FORMULATION FOR THE NAVIER-STOKES EQUATIONS IN NONHYDROSTATIC MESOSCALE MODELING

MARCO RESTELLI\* AND FRANCIS X. GIRALDO†

**Abstract.** A Discontinuous Galerkin (DG) finite element formulation is proposed for the solution of the compressible Navier–Stokes equations for a vertically stratified fluid, which are of interest in mesoscale nonhydrostatic atmospheric modeling. The resulting scheme naturally ensures conservation of mass, momentum and energy. A semi-implicit time integration approach is adopted to improve the efficiency of the scheme with respect to explicit Runge–Kutta time integration strategies usually employed in the context of DG formulations. A method is also presented to reformulate the resulting linear system as a pseudo-Helmholtz problem. In doing this, we obtain a DG discretization closely related to those proposed for the solution of elliptic problems, and we show how to take advantage of numerical integration to increase the efficiency of the solution algorithm. The resulting numerical formulation is then validated on a collection of classical two-dimensional test cases, including density driven flows and mountain wave simulations.

**Key words.** compressible flows, Euler equations, Navier–Stokes equations, discontinuous Galerkin finite element method, semi-implicit time discretizations

**AMS subject classifications.** 65M60, 65M70, 35L65, 86A10

**1. Introduction.** In recent years, great attention has been devoted to the Discontinuous Galerkin (DG) finite element method in the context of geophysical fluid dynamics applications. This is motivated by the fact that the DG framework simultaneously provides: a high-order discretization, great flexibility in the choice of the computational grid, discrete balance relations, robustness with respect to unphysical oscillations, and compact computational stencils, which are a key element in order to exploit distributed-memory parallel computers with up to tens of thousands of processors. Without attempting to provide a complete review of the literature, we mention here [43, 2, 28, 35, 27], where DG shallow water models are presented. The application of the DG method to compressible, nonhydrostatic atmospheric flows, using the Navier–Stokes equations or, when the flow is assumed to be inviscid, the Euler equations, is then considered in [29], where it is shown that the method represents a good candidate for the development of numerical climate and weather models. In the present paper, we continue the study initiated in [29] by focusing on the aspect of the time discretization which is, in fact, the most penalizing drawback of the DG method due to its high computational cost. This latter cost stems from the following reasons: the need of a complete independent set of points for each element to span the local polynomial space; a stricter time-step than in continuous methods due to the upwinding mechanism in the numerical flux; and the fact that all previous applications have been confined to explicit time-integration. Our goal is to remedy the last two points. More precisely, the main purpose of this article is to show that it is possible to use a semi-implicit (SI) time stepping method in combination with a DG spatial discretization, thus improving the computational efficiency, without affecting the positive features of the method. The SI approach was first introduced in [34] for the solution of the primitive hydrostatic equations. Modifications were proposed

---

\*Ozean im Erdsystem, Max–Planck–Institut für Meteorologie, Bundesstraße 53, 20146 Hamburg, Germany (marco.restelli@zmaw.de).

†Department of Applied Mathematics, Naval Postgraduate School, Monterey, CA 93943, USA (fxgiraldo@nps.edu).

in [10] for the hydrostatic case and the technique was then extended to the complete non hydrostatic Euler equations in [49, 18, 48], with implicit treatment of the acoustic and gravity waves. Since then, the method has been widely employed in climate and weather prediction models, and we refer to [39, 7, 26] for further details. However, to our knowledge, a SI time discretization has never been used in combination with a DG spatial discretization, and the SI-DG formulation described in the present paper represents a novel contribution. This formulation, moreover, besides being suited for atmospheric flow problems, may be useful also in the context of smaller scale, low Mach number fluid dynamics simulations. We notice here that our scheme is different from the one proposed in [21] despite the fact that both are referred to as “semi-implicit Discontinuous Galerkin” formulations. The method proposed by Dolejší and Feistauer relies in fact on a careful handling of the nonlinear problem arising from a fully implicit time stepping, and a key ingredient of the method is the choice of a particular numerical flux. This approach is thus suitable for high Mach number flows. On the contrary, in our approach only the terms responsible for acoustic and gravity waves are treated implicitly, and there is much freedom in the choice of the numerical flux. As a result, the scheme we propose is less restrictive in regards to the numerical flux and effective for the treatment of low Mach number flows. A final comment is in order concerning the solution algorithm for the linear system associated with the SI time discretization. We show how it is possible to reformulate such a system as a pseudo-Helmholtz problem, the discretization of which is closely related to the Local Discontinuous Galerkin (LDG) methods proposed in [13, 4] for elliptic problems. This reformulation yields a significant efficiency improvement.

An outline of the paper is as follows. In § 2 the governing equations are introduced. Section 3 deals with the SI time discretization, while the DG spatial discretization is presented in § 4. The space-time fully discretized problem is then summarized in § 5. In particular, a method to reformulate the resulting linear system as a pseudo-Helmholtz problem is illustrated in § 5.2. The numerical validation of the proposed formulation is carried out in § 6. Finally, conclusions and future developments are discussed in § 7.

**2. Governing Equations.** In this section, we introduce the continuous equations representing the mathematical model for the atmospheric flow problem considered in the present paper. Various alternative equation sets have been proposed in the literature to describe the nonhydrostatic flow of a dry, stratified atmosphere. In [29] three different equation sets are examined by comparing the results of five spectral element and discontinuous Galerkin codes, and it is found that the conservative Navier–Stokes equations using density, momentum and total energy as prognostic variables represent one of the most effective choices as far as accuracy is concerned. In addition, the fact that such an equation set is in conservation form, even when taking into account viscous stresses, makes it a suitable starting point for the construction of a numerical scheme endowed with discrete conservation properties. For these reasons, this equation set is considered in the present work. Restricting ourselves for simplicity to a two dimensional case in the vertical  $(x, z)$  plane, and neglecting the Coriolis terms, we end up with the following system (see [5]):

$$\frac{\partial \mathbf{q}}{\partial t} + \nabla \cdot \mathcal{F}^e(\mathbf{q}) - \nabla \cdot \mathcal{F}^v(\mathbf{q}, \nabla \mathbf{q}) = \mathbf{G}(\mathbf{q}), \quad (2.1)$$

where each term is defined as follows:  $\mathbf{q} = (\rho, \mathbf{V}^T, E)^T$  are the conserved quantities,  $\rho$  is the density and, letting  $\mathbf{v}$  denote the velocity field,  $c_v$  and  $g$  denote the specific

heat for constant volume and the gravitational constant, respectively,  $T$  denote the temperature and  $e = c_v T + \frac{1}{2} \mathbf{v} \cdot \mathbf{v} + gz$  represent the total energy,  $\mathbf{V} = \rho \mathbf{v}$  is the momentum and  $E = \rho e$  the energy density. The inviscid and viscous fluxes and the source term in (2.1) are given by

$$\mathcal{F}^e(\mathbf{q}) = \left\{ \begin{array}{c} \mathbf{V} \\ \frac{1}{\rho} \mathbf{V} \otimes \mathbf{V} + p \mathcal{I} \\ \frac{1}{\rho} H \mathbf{V} \end{array} \right\}, \quad \mathcal{F}^v(\mathbf{q}, \nabla \mathbf{q}) = \left\{ \begin{array}{c} 0 \\ \mathcal{F}_{\mathbf{V}}^v(\mathbf{q}, \nabla \mathbf{q}) \\ \mathbf{F}_E^v(\mathbf{q}, \nabla \mathbf{q}) \end{array} \right\}, \quad \mathbf{G}(\mathbf{q}) = \left\{ \begin{array}{c} 0 \\ \rho \mathbf{g} \\ 0 \end{array} \right\}.$$

where  $p$  is the pressure,  $\mathbf{g} = -g\mathbf{k}$ , with  $\mathbf{k} = (0, 1)^T$ ,  $H = E + p$  is the enthalpy, and the viscous fluxes are defined as

$$\mathcal{F}_{\mathbf{V}}^v = \mu [\nabla \mathbf{v} + \nabla \mathbf{v}^T + \lambda \nabla \cdot \mathbf{v} \mathcal{I}], \quad \mathbf{F}_E^v = \frac{\mu c_p}{Pr} \nabla T + \mathbf{v} \cdot \mathcal{F}_{\mathbf{V}}^v,$$

$\mu$  and  $\lambda$  denoting the two viscosity coefficients,  $c_p$  denoting the specific heat for constant pressure and  $Pr$  being the Prandtl number. Using the Stokes hypothesis, we can set  $\lambda = -\frac{2}{3}$ . Notice that, although for practical applications a turbulence closure relation has to be considered to define the viscosity coefficients, in the present work we assume that these latter are known constants. Closure of system (2.1) is obtained through the equation of state, which, in terms of the solution variables, is written as

$$p = \frac{R}{c_v} \left( E - \frac{1}{2} \frac{V^2}{\rho} - \rho g z \right), \quad (2.2)$$

with  $R = c_p - c_v$ . Equations (2.1) reduce to the Euler equations when  $\mu = 0$ ,  $\lambda = 0$ .

When solving system (2.1) for atmospheric flows, it can be expected that the flow is nearly hydrostatic, i.e. in the vertical momentum equation the two terms  $\frac{\partial p}{\partial z}$  (from the inviscid flux) and  $\rho g$  (from the source term) are much larger than the remaining ones. This can cause instabilities in the numerical approximation of the problem, due to cancellation of significant digits. To avoid this effect, problem (2.1) is usually reformulated in terms of deviations from a constant-in-time reference state (see [22] and, for an alternative, more sophisticated approach, [8]). Thus, we introduce  $\bar{\mathbf{q}} = (\bar{\rho}, \bar{\mathbf{V}}^T, \bar{E})^T$  and  $\bar{p} = p(\bar{\rho}, \bar{\mathbf{V}}, \bar{E})$  such that  $\bar{\mathbf{V}} = 0$ ,  $\frac{\partial \bar{p}}{\partial x} = 0$ ,  $\frac{\partial \bar{E}}{\partial x} = 0$  (also implying  $\frac{\partial \bar{p}}{\partial x} = 0$ ) and

$$\frac{d\bar{p}}{dz} = -\bar{\rho} g. \quad (2.3)$$

Upon defining  $\mathbf{q}' = \mathbf{q} - \bar{\mathbf{q}}$  and  $p' = p - \bar{p}$ , we obtain

$$\frac{\partial \mathbf{q}'}{\partial t} + \nabla \cdot \mathcal{F}^{e'}(\mathbf{q}) - \nabla \cdot \mathcal{F}^v(\mathbf{q}, \nabla \mathbf{q}) = \mathbf{G}(\mathbf{q}'), \quad (2.4)$$

where

$$\mathcal{F}^{e'}(\mathbf{q}) = \left\{ \begin{array}{c} \mathbf{V} \\ \frac{1}{\rho} \mathbf{V} \otimes \mathbf{V} + p' \mathcal{I} \\ \frac{1}{\rho} H \mathbf{V} \end{array} \right\}.$$

Equation (2.2) allows for an expression of  $p'$  which is independent from  $\bar{\rho}$ ,  $\bar{E}$

$$p' = \frac{R}{c_v} \left( E' - \frac{1}{2} \frac{V'^2}{\rho} - \rho' g z \right),$$

so that no cancellation problems occur in evaluating the pressure perturbation. Problem (2.4) has the advantage that all the terms in the vertical momentum equations are of the same order of magnitude. For this reason, in the following we will always use (2.4) instead of (2.1), and we will drop the primes for simplicity.

**2.1. Treatment of the Open Boundary Conditions.** In practical applications, it is usually necessary to truncate the computational domain with artificial boundaries, not corresponding to any physical entity. Ideally, an “open boundary” condition is desired on these boundaries, avoiding any reflection of outgoing signals. A simple and robust solution is represented by an *absorbing layer*, also known as a *sponge layer*, as discussed in [32, 23]. In these references, a method is described to optimize the structure of the absorbing layer in the case where the primitive variable formulation is considered, i.e. when the prognostic variables are Exner pressure, velocity and potential temperature. To apply these results to the conservative formulation (2.4), we can in principle perform a change of variables from conservative to primitive variables, apply the damping coefficients and then transform back to conservative variables. In practice, this can be done as follows: denoting by  $\mathbf{q}_b = (\rho_b, \mathbf{V}_b^T, E_b)^T$  a known boundary datum, we modify system (2.4) to obtain

$$\frac{\partial \mathbf{q}}{\partial t} = \mathcal{S}^{NS}(\mathbf{q}) - T^{cv}(\mathbf{q} - \mathbf{q}_b), \quad (2.5)$$

with  $\mathcal{S}^{NS}(\mathbf{q}) = -\nabla \cdot \mathcal{F}^e(\mathbf{q}) + \nabla \cdot \mathcal{F}^v(\mathbf{q}, \nabla \mathbf{q}) + \mathbf{G}(\mathbf{q})$  and

$$T^{cv} = M^{-1} T^{pv} M. \quad (2.6)$$

In (2.6),  $M$  is a  $4 \times 4$  matrix representing the linearized transformation between conservative variables and primitive variables, the linearization being performed in a neighborhood of  $\mathbf{q}_b$ , while  $T^{pv}$  is a diagonal matrix whose four entries are computed as in [32, 23]. Once the absorbing layer has been introduced within the computational domain, the particular boundary condition prescribed on the boundary of the computational domain itself has in practice no effect on the computed solution, so that, because of the ease of implementation, we impose the Dirichlet condition  $\mathbf{q} = \mathbf{q}_b$ . We notice that, although introducing an absorbing layer is a common solution to handle non-reflecting boundary conditions, more sophisticated alternatives are possible. In particular, we are currently exploring Higdon-type high-order boundary conditions [20] which we reserve for future work since this topic is beyond the scope of the present paper.

**2.2. Identification of the fast waves in the model.** In order to devise a semi-implicit time integration scheme for system (2.4), it is first necessary to identify the terms responsible for the fastest waves in the model, i.e. acoustic and gravity waves. In fact, in the semi-implicit time integration procedure, an implicit treatment will be selectively applied to such terms, while an explicit approach will be adopted for the remaining ones. Following [33], we identify these terms as the divergence of the mass in the continuity equation, the pressure gradient and the buoyancy term in the momentum equation and the divergence of the enthalpy flux in the energy equation (see also the simplified stability analysis in [37]). To linearize these terms, we introduce the linear operator

$$\mathcal{L}^{NS}(\mathbf{q}) = -\nabla \cdot \mathcal{F}^{\mathcal{L}}(\mathbf{q}) + \mathbf{G}(\mathbf{q}) \quad (2.7)$$

with

$$\mathcal{F}^{\mathcal{L}}(\mathbf{q}) = \left\{ \begin{array}{c} \mathbf{V} \\ \frac{R}{c_v} (E - \rho g z) \mathcal{I} \\ \bar{h} \mathbf{V} \end{array} \right\}$$

and  $\bar{h} = \frac{1}{\rho} (\bar{E} + \bar{p})$ . The linearized form (2.7) represents the basis for the definition of the linear problem which will be discussed in Sect. 4.4.

**3. Temporal Discretization.** In this section we discuss the semi-implicit method adopted for the time discretization of system (2.5). We notice that, although the SI approach is usually considered in combination with either the Crank–Nicolson or the leapfrog time integration schemes, following the abstract formulation of [26] it is possible to include other time integration schemes, such as the backward difference scheme presented in [31] and summarized in the sequel. We thus consider the abstract problem

$$\frac{d\mathbf{q}}{dt} = \widetilde{\mathcal{F}}(\mathbf{q}), \quad (3.1)$$

to be solved in  $(0, T_{fin}]$  with a suitable initial condition, define an affine operator  $\widetilde{\mathcal{A}}$  such that  $\widetilde{\mathcal{A}}\mathbf{q} \approx \widetilde{\mathcal{F}}(\mathbf{q})$  and set

$$\frac{d\mathbf{q}}{dt} = \left\{ \widetilde{\mathcal{F}}(\mathbf{q}) - \widetilde{\mathcal{A}}\mathbf{q} \right\} + \widetilde{\mathcal{A}}\mathbf{q}. \quad (3.2)$$

The main idea is now to treat the term in braces explicitly, while the remaining term will be treated implicitly. Notice that problem (2.5) can be recast in the form (3.1) by setting  $\widetilde{\mathcal{F}}(\mathbf{q}) = \mathcal{S}^{NS}(\mathbf{q}) - T^{cv}(\mathbf{q} - \mathbf{q}_b)$ . To allow for more flexibility in the treatment of the damping term, it is also convenient to split the affine operator  $\widetilde{\mathcal{A}}$  as  $\widetilde{\mathcal{A}} = \mathcal{A} + \mathcal{A}^0$ , and set  $\mathcal{A}\mathbf{q} = \mathcal{L}\mathbf{q} + \mathbf{f}$  and  $\mathcal{A}^0\mathbf{q} = \mathcal{L}^0\mathbf{q} + \mathbf{f}^0$ , where  $\mathbf{f}$  and  $\mathbf{f}^0$  are assumed to be constant in time. Eq. (3.2) can now be written as

$$\frac{d\mathbf{q}}{dt} = \left\{ \mathcal{S}(\mathbf{q}) - \mathcal{L}\mathbf{q} \right\} + \mathcal{L}\mathbf{q} + \mathcal{L}^0\mathbf{q} + \mathbf{f}^0, \quad (3.3)$$

where  $\mathcal{S}(\mathbf{q}) = \widetilde{\mathcal{F}}(\mathbf{q}) - \mathcal{A}^0\mathbf{q}$ . Choosing now a time-step  $\Delta t$ , letting  $t^n = n\Delta t$ , with  $n = 0, \dots, T_{fin}/\Delta t$ , and denoting by  $\mathbf{q}^n$  the approximate solution at time level  $t^n$ , the discretization of (3.3) is constructed as follows:

$$\begin{aligned} \frac{d\mathbf{q}}{dt} &\approx \frac{1}{\gamma\Delta t} \left[ \mathbf{q}^{n+1} - \sum_{m=0}^1 \alpha_m \mathbf{q}^{n-m} \right] \\ \left\{ \mathcal{S}(\mathbf{q}) - \mathcal{L}\mathbf{q} \right\} &\approx \sum_{m=0}^1 \beta_m \left( \mathcal{S}(\mathbf{q}^{n-m}) - \mathcal{L}\mathbf{q}^{n-m} \right) \\ \mathcal{L}\mathbf{q} &\approx \sum_{m=-1}^1 \sigma_m \mathcal{L}\mathbf{q}^{n-m} \\ \mathcal{L}^0\mathbf{q} &\approx \mathcal{L}^0\mathbf{q}^{n+1} \end{aligned} \quad (3.4)$$

for suitable coefficients  $\gamma$ ,  $\alpha_m$ ,  $\beta_m$  and  $\sigma_m$ . Notice that, for consistency, it is required that  $\sum_m \alpha_m = \sum_m \beta_m = \sum_m \sigma_m = 1$ . Typically, the operator  $\mathcal{L}$  is chosen in such a

Method	$\alpha_0$	$\alpha_1$	$\gamma$	$\beta_0$	$\beta_1$	$\sigma_{-1}$	$\sigma_0$	$\sigma_1$
TM	1	0	1	1	0	$\theta$	$1 - \theta$	0
LF2	0	1	2	1	0	$\theta$	0	$1 - \theta$
BDF2	4/3	-1/3	2/3	2	-1	1	0	0

TABLE 3.1

$\theta$ -method (TM), leapfrog (LF2), and backward difference (BDF2) time integration schemes and their associated coefficients in the context of Eq. (3.4).

way that, for a particular range of  $\mathbf{q}$ , the term  $\mathcal{S} - \mathcal{L}$  vanishes, and time integration is performed with the implicit scheme (3.4)<sub>1,3,4</sub>. In Tab. 3.1 it is shown how to recover some classical time marching schemes by properly choosing the coefficients in (3.4), namely the  $\theta$ -method, the leap-frog method and the backward difference scheme proposed in [31], while a thorough analysis of such schemes can be found in [26]. Having completely defined our time integration method, it is important to notice that, in most numerical weather prediction codes, the semi-implicit method is usually implemented as an implicit correction to an explicit predictor substep [39]. In our case, this leads to the following algorithm:

(i) compute the explicit predictor step

$$\tilde{\mathbf{q}}^{ex} = \sum_{m=0}^1 \alpha_m \mathbf{q}^{n-m} + \gamma \Delta t \sum_{m=0}^1 \beta_m \mathcal{S}(\mathbf{q}^{n-m});$$

(ii) let  $\rho_m = \sigma_m - \beta_m$ , with  $\beta_{-1} = 0$  and compute  $\mathbf{q}^* = \rho_{-1} \tilde{\mathbf{q}}^{ex} + \sum_{m=0}^1 \rho_m \mathbf{q}^{n-m}$ ;

(iii) let  $\mathcal{B} = (\mathcal{I} - \gamma \Delta t \mathcal{L}^0)^{-1}$ , where  $\mathcal{I}$  is the identity and compute the implicit corrector step

$$\begin{aligned} (\mathcal{I} - \rho_{-1}(\gamma \Delta t \mathcal{B} \mathcal{L})) \mathbf{q}_{tt} &= \mathcal{B} \mathbf{q}^* - (\gamma \Delta t \mathcal{B} \mathcal{L}^0) \left( \sum_{m=0}^1 \rho_m \mathbf{q}^{n-m} \right) \\ &\quad + \rho_{-1}(\gamma \Delta t \mathcal{B} \mathbf{f}^0); \end{aligned}$$

Notice that  $\mathbf{q}_{tt}$  is an approximation of  $\frac{\partial^2 \mathbf{q}}{\partial t^2}$  (see [26]).

(iv) update the solution by setting  $\mathbf{q}^{n+1} = \frac{1}{\rho_{-1}} \left( \mathbf{q}_{tt} - \sum_{m=0}^1 \rho_m \mathbf{q}^{n-m} \right)$ .

**4. Spatial Discretization.** In this section, we address the spatial discretization of (2.5) by resorting to a high-order, nodal, DG formulation. The general framework for such discretization is provided by [6, 5], while we refer to [28, 27, 30] for the aspects specifically related to the high-order approximation.

**4.1. Notation.** Let  $\Omega$  be an open bounded domain of  $\mathbb{R}^2$ , with boundary  $\partial\Omega$  and outward unit normal vector  $\mathbf{n}_{\partial\Omega}$ , and let  $\mathcal{T}_h$  denote a partition of  $\Omega$  into  $\mathcal{N}_{el}$  nonoverlapping curvilinear quadrilateral elements  $K$  which are images of the reference element  $\hat{K} = [-1, 1]^2$  under smooth, bijective maps  $\mathcal{F}_K$

$$\forall K \in \mathcal{T}_h : \quad K = \mathcal{F}_K(\hat{K}).$$

The diameter of  $K$  is  $h_K$  and we let  $h = \max_{K \in \mathcal{T}_h} h_K$ . The set of the edges  $e$  of the triangulation is denoted by  $\mathcal{E}_h$ . Let  $\partial K$  and  $\mathbf{n}_{e, \partial K}$  denote the boundary of  $K \in \mathcal{T}_h$  and the outward unit normal vector on each edge  $e \in \partial K$ , respectively, and  $\partial \hat{K}$  and

$\mathbf{n}_{\widehat{e}, \partial \widehat{K}}$  denote the boundary and the outward unit normal vector for the reference element  $\widehat{K}$ . The notation  $\mathbf{x} = \mathcal{T}_K(\boldsymbol{\xi})$ , with  $\mathbf{x} = (x, z) \in \Omega$ ,  $\boldsymbol{\xi} = (\xi, \zeta) \in \widehat{K}$  will be used. We also associate with each local map the Jacobian  $J_K = \frac{d\mathcal{T}_K}{d\boldsymbol{\xi}}$  and the determinant  $|J_K|$ . Although not essential, we will assume that  $\mathcal{T}_h$  is conforming, that is, given  $K_1, K_2 \in \mathcal{T}_h$  we either have that  $K_1 \cap K_2$  is empty, or it is a vertex or a complete edge  $e \in \mathcal{E}_h$ . Following the usual notation in the context of DG formulation, we now define averages and jumps (see [16, 4]). Letting thus  $\chi_h$  denote a generic function piecewise continuous on  $\mathcal{T}_h$ , for a given element  $K$ , edge  $e \subset \partial K$  and point  $\mathbf{x} \in e$  we define

$$\chi_h(\mathbf{x}^{int(K)}) = \lim_{\substack{\mathbf{y} \rightarrow \mathbf{x} \\ \mathbf{y} \in \overset{\circ}{K}}} \chi_h(\mathbf{y}), \quad \chi_h(\mathbf{x}^{ext(K)}) = \lim_{\substack{\mathbf{y} \rightarrow \mathbf{x} \\ \mathbf{y} \notin K}} \chi_h(\mathbf{y}).$$

This definition can be extended to vector valued functions by applying it componentwise. For  $e = \partial K \cap \partial K'$ ,  $\mathbf{x} \in e$ , the average and jump for a scalar function  $\chi_h$  and vector function  $\mathbf{r}_h$  piecewise continuous on  $\mathcal{T}_h$  are defined, respectively, as follows:

$$\begin{aligned} \{\chi_h\}(\mathbf{x}) &= \frac{1}{2} \left( \chi_h(\mathbf{x}^{int(K)}) + \chi_h(\mathbf{x}^{int(K')}) \right) \\ \{\mathbf{r}_h\}(\mathbf{x}) &= \frac{1}{2} \left( \mathbf{r}_h(\mathbf{x}^{int(K)}) + \mathbf{r}_h(\mathbf{x}^{int(K')}) \right) \\ \llbracket \chi_h \rrbracket(\mathbf{x}) &= \chi_h(\mathbf{x}^{int(K)}) \mathbf{n}_{e, \partial K} + \chi_h(\mathbf{x}^{int(K')}) \mathbf{n}_{e, \partial K'} \\ \llbracket \mathbf{r}_h \rrbracket(\mathbf{x}) &= \mathbf{r}_h(\mathbf{x}^{int(K)}) \otimes \mathbf{n}_{e, \partial K} + \mathbf{r}_h(\mathbf{x}^{int(K')}) \otimes \mathbf{n}_{e, \partial K'}. \end{aligned} \tag{4.1}$$

Notice that (4.1)<sub>4</sub> differs from the usual definition of the jump for a vector valued function, and this latter can be recovered as  $\llbracket \mathbf{r}_h \rrbracket = \text{Tr}(\llbracket \mathbf{r}_h \rrbracket)$ . Finally, we let  $\max \{\chi_h(\mathbf{x})\} = \max \left\{ \chi_h(\mathbf{x}^{int(K)}), \chi_h(\mathbf{x}^{int(K')}) \right\}$ .

**4.2. High-Order Polynomial Space.** The logically square structure of the reference element  $\widehat{K}$  significantly simplifies the construction of high-order polynomial bases, since the multidimensional basis can be obtained as a tensor-product of the one-dimensional basis. For an integer  $k \geq 1$ , letting  $\mathbb{P}_k([a, b])$  denote the space of polynomial functions of degree less than or equal to  $k$  on  $[a, b]$ , we introduce the following two bases for  $\mathbb{P}_k([-1, 1])$ :  $\{\varphi_i(\xi)\}_{i=0}^k$  is the Lagrangian (i.e. nodal) basis associated with an arbitrary set of nodes  $\xi_i \in [-1, 1]$ , while  $\{\psi_i(\xi)\}_{i=0}^k$  is the Legendre (i.e. modal) basis (see [11]). We also define

$$\widehat{\Phi}_{ij}(\boldsymbol{\xi}) = \varphi_i(\xi) \varphi_j(\zeta) \quad \text{and} \quad \Phi_{K, ij}(\mathbf{x}) = \begin{cases} (\widehat{\Phi}_{ij} \circ \mathcal{T}_K^{-1})(\mathbf{x}), & \mathbf{x} \in K \\ 0, & \mathbf{x} \notin K \end{cases}.$$

For simplicity, a cumulative index  $I$ , ranging from 1 to  $\mathcal{N} = (k+1)^2 \mathcal{N}_{el}$ , is also biunivocally associated with the indexes  $(K, ij)$ . Although, in principle, several choices for the nodes  $\xi_i$  are possible, a convenient one is represented by the Legendre–Gauss–Lobatto (LGL) points, defined as the roots of the polynomial  $(1 - \xi^2) \psi'_k(\xi)$ . As a matter of fact, these points are endowed with a Gaussian quadrature rule that can be exploited to improve the efficiency of the resulting scheme (see [11]). The finite element space is now defined as  $V_h = \text{span} \{\Phi_I\}$ ,  $I = 1, \dots, \mathcal{N}$ . Notice that functions in  $V_h$  are in general discontinuous across edges  $e \in \mathcal{E}_h$ .



As it will be clear from the forthcoming sections, the DG formulation requires the evaluation of both two-dimensional and one-dimensional integrals on  $K$  and  $\partial K$ , respectively. To this end, following [28] the following approximate quadrature rules will be adopted

$$\int_K \chi(\mathbf{x}) d\mathbf{x} = \int_{\widehat{K}} \chi(\mathbf{x}(\boldsymbol{\xi})) |J_K(\boldsymbol{\xi})| d\boldsymbol{\xi} \approx \sum_{i,j=0}^k \chi(\mathbf{x}(\xi_i, \zeta_j)) |J_K(\xi_i, \zeta_j)| \widehat{w}_i \widehat{w}_j \quad (4.2)$$

and

$$\begin{aligned} \int_{\partial K} \chi(\sigma) d\sigma &= \sum_{\widehat{e} \in \partial \widehat{K}} \int_{\widehat{e}} \chi(\mathbf{x}(\widehat{\sigma})) |J_K(\widehat{\sigma})| \|J_K^{-T}(\widehat{\sigma}) \mathbf{n}_{\widehat{e}, \partial \widehat{K}}\|_2 d\widehat{\sigma} \\ &\approx \sum_{i=0}^k \chi(\mathbf{x}(\xi_i, \zeta_0)) |J_K(\xi_i, \zeta_0)| \|J_K^{-T}(\xi_i, \zeta_0) \mathbf{n}_{\widehat{e}_1, \partial \widehat{K}}\|_2 \widehat{w}_i \\ &\quad + \sum_{j=0}^k \chi(\mathbf{x}(\xi_k, \zeta_j)) |J_K(\xi_k, \zeta_j)| \|J_K^{-T}(\xi_k, \zeta_j) \mathbf{n}_{\widehat{e}_2, \partial \widehat{K}}\|_2 \widehat{w}_j \\ &\quad + \sum_{i=0}^k \chi(\mathbf{x}(\xi_i, \zeta_k)) |J_K(\xi_i, \zeta_k)| \|J_K^{-T}(\xi_i, \zeta_k) \mathbf{n}_{\widehat{e}_3, \partial \widehat{K}}\|_2 \widehat{w}_i \\ &\quad + \sum_{j=0}^k \chi(\mathbf{x}(\xi_0, \zeta_j)) |J_K(\xi_0, \zeta_j)| \|J_K^{-T}(\xi_0, \zeta_j) \mathbf{n}_{\widehat{e}_4, \partial \widehat{K}}\|_2 \widehat{w}_j \end{aligned} \quad (4.3)$$

where  $\chi$  is a generic function piecewise continuous on  $\mathcal{T}_h$ ,  $\|\cdot\|_2$  is the Euclidean norm of a vector,  $\xi_i$  and  $\zeta_i$  are Legendre–Gauss–Lobatto points previously introduced and  $\widehat{w}_i$  are the associated weights, defined as

$$\widehat{w}_i = \frac{2}{k(k+1)} \left( \frac{1}{\psi_k(\xi_i)} \right).$$

In the following, for  $i, j = 0, \dots, k$ , we will let:

$$\begin{aligned} w_{K,ij} &= |J_K(\xi_i, \zeta_j)| \widehat{w}_i \widehat{w}_j, \\ \omega_{K,ij}^e &= \begin{cases} |J_K(\xi_i, \zeta_j)| \|J_K^{-T}(\xi_i, \zeta_j) \mathbf{n}_{\widehat{e}, \partial \widehat{K}}\|_2 \widehat{w}_i, & (j, \widehat{e}) \in \{(0, \widehat{e}_1), (k, \widehat{e}_3)\} \\ |J_K(\xi_i, \zeta_j)| \|J_K^{-T}(\xi_i, \zeta_j) \mathbf{n}_{\widehat{e}, \partial \widehat{K}}\|_2 \widehat{w}_j, & (i, \widehat{e}) \in \{(0, \widehat{e}_2), (k, \widehat{e}_4)\} \\ 0 & \text{otherwise.} \end{cases} \end{aligned}$$

Notice that the degree of exactness of the quadrature rules (4.2) and (4.3) is  $2k - 1$ . Nonetheless, as discussed in [28], this approximation does not spoil the order of accuracy of the resulting DG formulation.

**4.3. Discontinuous Galerkin Discretization.** We first rewrite (2.5) introducing the auxiliary variable  $\mathcal{S}$  as:

$$\begin{cases} \frac{\partial \mathbf{q}}{\partial t} = -\nabla \cdot \mathcal{F}^e(\mathbf{q}) + \nabla \cdot \mathcal{F}^v(\mathbf{q}, \mathcal{S}) + \mathbf{G}(\mathbf{q}) - T^{cv}(\mathbf{q} - \mathbf{q}_b) \\ \mathcal{S} - \nabla \mathbf{q} = 0 \end{cases} \quad (4.4)$$

to be solved in  $\Omega \times (0, T_{fin}]$  with suitable initial and boundary conditions. An approximation  $(\mathbf{q}_h, \mathcal{S}_h) = (\mathbf{q}_h(\mathbf{x}, t), \mathcal{S}_h(\mathbf{x}, t))$  to the solution  $(\mathbf{q}(\mathbf{x}, t), \mathcal{S}(\mathbf{x}, t))$  of (4.4) is sought, such that  $(\mathbf{q}_h, \mathcal{S}_h) \in (V_h)^4 \times (V_h)^8$  at each time level. In the following, for the sake of clarity we will often omit the dependence of  $\mathbf{q}_h$  and  $\mathcal{S}_h$  on  $(\mathbf{x}, t)$ . Also, all products, differential operators and average and jump operators are intended to be applied separately to each density, momentum and energy component of their arguments. Multiplying the two equations (4.4) by test functions  $\chi_h \in (V_h)^4$  and  $\mathcal{R}_h \in (V_h)^8$ , respectively, integrating over  $K \in \mathcal{T}_h$  and replacing the exact solution by its approximation, we have:

$$\left\{ \begin{array}{l} \frac{d}{dt} \int_K \mathbf{q}_h \chi_h \, d\mathbf{x} = - \int_K \nabla \cdot [\mathcal{F}^e(\mathbf{q}_h) - \mathcal{F}^v(\mathbf{q}_h, \mathcal{S}_h)] \chi_h \, d\mathbf{x} \\ \quad + \int_K [\mathbf{G}(\mathbf{q}_h) - T^{cv}(\mathbf{q}_h - \mathbf{q}_b)] \chi_h \, d\mathbf{x}, \quad \forall \chi_h \in (V_h)^4 \\ \int_K \mathcal{S}_h \cdot \mathcal{R}_h \, d\mathbf{x} - \int_K \nabla \mathbf{q}_h \cdot \mathcal{R}_h \, d\mathbf{x} = 0, \quad \forall \mathcal{R}_h \in (V_h)^8. \end{array} \right.$$

Then, formally integrating by parts and introducing the numerical fluxes  $\widehat{\mathcal{F}}^e(\mathbf{q}_h)$ ,  $\widehat{\mathbf{q}}(\mathbf{q}_h, \mathcal{S}_h)$  and  $\widehat{\mathcal{S}}(\mathbf{q}_h, \mathcal{S}_h)$ , we obtain the following discrete problem:  
find  $(\mathbf{q}_h(\cdot, t), \mathcal{S}_h(\cdot, t)) \in (V_h)^4 \times (V_h)^8$  such that for all  $t \in [0, T_{fin}]$  and  $\forall K \in \mathcal{T}_h$ :

$$\left\{ \begin{array}{l} \frac{d}{dt} \int_K \mathbf{q}_h \chi_h \, d\mathbf{x} = \int_K [\mathcal{F}^e(\mathbf{q}_h) - \mathcal{F}^v(\mathbf{q}_h, \mathcal{S}_h)] \cdot \nabla \chi_h \, d\mathbf{x} \\ \quad - \int_{\partial K} [\widehat{\mathcal{F}}^e(\mathbf{q}_h) - \mathcal{F}^v(\widehat{\mathbf{q}}, \widehat{\mathcal{S}})] \cdot \mathbf{n}_{\partial K} \chi_h \, d\sigma \\ \quad + \int_K [\mathbf{G}(\mathbf{q}_h) - T^{cv}(\mathbf{q}_h - \mathbf{q}_b)] \chi_h \, d\mathbf{x}, \quad \forall \chi_h \in (V_h)^4 \\ \int_K \mathcal{S}_h \cdot \mathcal{R}_h \, d\mathbf{x} + \int_K \mathbf{q}_h \nabla \cdot \mathcal{R}_h \, d\mathbf{x} - \int_{\partial K} \widehat{\mathbf{q}} \mathbf{n}_{\partial K} \cdot \mathcal{R}_h \, d\sigma = 0, \quad \forall \mathcal{R}_h \in (V_h)^8. \end{array} \right. \quad (4.5)$$

Specification of the numerical fluxes completes now the definition of the scheme. Concerning the hyperbolic flux, we consider here the Rusanov flux (see [41, 50])

$$\widehat{\mathcal{F}}^e(\mathbf{q}_h) = \{\mathcal{F}^e(\mathbf{q}_h)\} + \frac{|\lambda|}{2} \llbracket \mathbf{q}_h \rrbracket \quad (4.6)$$

where  $|\lambda| = \max\{|\mathbf{v}_h \cdot \mathbf{n}| + a_h\}$ ,  $\mathbf{v}_h$  and  $a_h$  denoting the wind velocity and sound speed associated with  $\mathbf{q}_h$ , respectively. The sound speed is in turn defined as  $a = \sqrt{\gamma RT}$ , with  $\gamma = c_p/c_v$ . We notice that more sophisticated choices than (4.6) are also possible, such as the HLL, HLLC or Roe's fluxes (see [50] and also [19] for comments about the effect of the numerical flux on the computed solution). Concerning the viscous terms, the Bassi and Rebay method of [5], which is a particular case of the Local Discontinuous Galerkin approach described in [17], is adopted. We thus set

$$\widehat{\mathbf{q}} = \{\mathbf{q}_h\}, \quad \widehat{\mathcal{S}} = \{\mathcal{S}_h\}. \quad (4.7)$$

**REMARK 4.1.** When  $T^{cv}$  vanishes, i.e. far from the open boundaries, the conservation properties of (4.5) follow naturally from its flux-form, which can be made explicit by taking the test function  $\chi_h$  equal to the characteristic function of  $K \in \mathcal{T}_h$ , yielding

$$\frac{d}{dt} \int_K \mathbf{q}_h \, d\mathbf{x} = - \int_{\partial K} [\widehat{\mathcal{F}}^e(\mathbf{q}_h) - \mathcal{F}^v(\widehat{\mathbf{q}}, \widehat{\mathcal{S}})] \cdot \mathbf{n}_{\partial K} \, d\sigma + \int_K \mathbf{G}(\mathbf{q}_h) \, d\mathbf{x},$$

and by noting that the numerical fluxes are single valued on  $\mathcal{E}_h$ . Notice also that discrete conservation is guaranteed regardless of the approximate evaluation of the area and boundary integrals.

We now take the test function  $\chi_h$  in  $(4.5)_1$  equal to  $\Phi_I$ . The left-hand side can be written as

$$\frac{d}{dt} \int_K \mathbf{q}_h \Phi_I \, d\mathbf{x} = M \frac{d\mathbf{q}_h}{dt}, \quad (4.8)$$

with

$$M_{IJ} = \int_K \Phi_I \Phi_J \, d\mathbf{x} = w_I \delta_{IJ}. \quad (4.9)$$

The right-hand side defines the operator

$$\begin{aligned} (\mathcal{S}_h^{NS}(\mathbf{q}_h))_I &= \int_K [\mathcal{F}^e(\mathbf{q}_h) - \mathcal{F}^v(\mathbf{q}_h, \mathcal{S}_h)] \cdot \nabla \Phi_I \, d\mathbf{x} \\ &\quad - \int_{\partial K} [\widehat{\mathcal{F}}^e(\mathbf{q}_h) - \mathcal{F}^v(\widehat{\mathbf{q}}, \widehat{\mathcal{S}})] \cdot \mathbf{n}_{\partial K} \Phi_I \, d\sigma + \int_K \mathbf{G}(\mathbf{q}_h) \Phi_I \, d\mathbf{x} \end{aligned} \quad (4.10)$$

for  $I = 1, \dots, \mathcal{N}$ ;  $\mathcal{S}_h^{NS}$  is the discrete counterpart of  $\mathcal{S}^{NS}$  in (2.5). Finally, the remaining terms, associated with the damping layer, will be considered in § 4.4.

**4.4. The Linear Problem.** Proceeding as done in § 2.2 to define  $\mathcal{L}^{NS}$  in (2.7) from  $\mathcal{S}^{NS}$  in (2.5), we identify within (4.10) the following linear operator

$$(\mathcal{L}_h^{NS} \mathbf{q}_h)_I = \int_K \mathcal{F}^{\mathcal{L}}(\mathbf{q}_h) \cdot \nabla \Phi_I \, d\mathbf{x} - \int_{\partial K} \widehat{\mathcal{F}}^{\mathcal{L}}(\mathbf{q}_h) \cdot \mathbf{n}_{\partial K} \Phi_I \, d\sigma + \int_K \mathbf{G}(\mathbf{q}_h) \Phi_I \, d\mathbf{x}, \quad (4.11)$$

for  $I = 1, \dots, \mathcal{N}$ . In (4.11) the linear numerical flux is

$$\widehat{\mathcal{F}}^{\mathcal{L}} = \{\mathcal{F}^{\mathcal{L}}\} + \frac{|\bar{\lambda}|}{2} \llbracket \mathbf{q}_h \rrbracket$$

where  $|\bar{\lambda}| = \bar{a} = \sqrt{\gamma R \bar{T}}$  and  $\bar{T}$  is the temperature of the reference state, which is assumed to be continuous function over  $\bar{\Omega}$ . We notice that the linear operator  $\mathcal{L}_h^{NS}$  represents the approximate counterpart, using the DG finite element method supplied with the Rusanov numerical flux, of the corresponding space-continuous operator  $\mathcal{L}^{NS}$  introduced in (2.7). In other words,  $\mathcal{L}^{NS}$  represents in itself a consistent DG discretization of the linearized Euler equations. In addition, in order to deal with the damping terms in  $(4.5)_1$ , we define

$$(\mathcal{L}_h^0 \mathbf{q}_h)_I = - \int_K T^{cv} \mathbf{q}_h \Phi_I \, d\mathbf{x}, \quad \mathbf{f}_I^0 = \int_K T^{cv} \mathbf{q}_b \Phi_I \, d\mathbf{x}, \quad (4.12)$$

for  $I = 1, \dots, \mathcal{N}$ .

**5. The Fully Discrete Problem.** The fully discrete space-time approximation of problem (2.5) is obtained by properly substituting into the multistep time advancing algorithm illustrated in § 3 the time derivative (4.8) and the discrete operators  $\mathcal{S}_h^{NS}(\mathbf{q}_h)$ ,  $\mathcal{L}_h^{NS} \mathbf{q}_h$ ,  $\mathcal{L}_h^0 \mathbf{q}_h$  and  $\mathbf{f}^0$  introduced in (4.10), (4.11) and (4.12), respectively. At each time level,  $\mathcal{S}_h$  is computed from  $(4.5)_2$ .

**5.1. Filtering the High-Frequency Modes.** The DG method using high-order basis functions can be regarded as a spectral element method with no continuity constraint among neighboring elements. Since high-order methods do not present any intrinsic numerical diffusion, they are prone to instabilities due to nonlinear mixing and the Gibbs phenomenon, particularly in the case of poorly resolved flows (see [9]). The usual way of dealing with this instability in the context of spectral formulations is to introduce a filtering operator which damps the high frequency modes without altering the low frequency modes. This is done by transforming from nodal representation to modal representation, applying a lowpass filter and then by transforming back to nodal representation. In the present paper, filtering is performed along the same lines as in [28], and the action of the filter is included in  $\mathcal{S}_h^{NS}$ .

**5.2. Solution Algorithm for the pseudo-Helmholtz Operator Problem.**

The linear system arising from the SI time discretization is usually dealt with by properly combining the continuity, momentum and energy equations, in such a way to obtain an algebraically equivalent problem of diffusion-reaction type, referred to as pseudo-Helmholtz operator problem, for the sole pressure variable. This equivalent reformulation has the computational advantage of reducing considerably the dimension of the problem; moreover, if an iterative solver is adopted, it produces a significant acceleration of the convergence rate and simplifies the definition of the stopping criterion. Based on these considerations, an extension of the above approach to the present semi-implicit DG setting is highly desirable, albeit being far from trivial. Nevertheless, such an extension can be made possible by conveniently exploiting the structure of the approximate quadrature rules (4.2) and (4.3). By doing so, one obtains a formulation that can be regarded as a LDG discretization of a diffusion-reaction problem for the pressure variable where the auxiliary flux unknown is statically condensed out by proper use of mass lumping. In this sense, the resulting discrete scheme shares some similarities with hybridized dual mixed methods where static condensation is the crucial approach to obtain a linear algebraic problem for the sole primal variable (see [3] for an introduction to static condensation at the discrete level, and [14, 15] for a more recent development on this subject).

For simplicity, we assume here that periodic boundary conditions are prescribed and we do not include the gravity terms into the implicit part of the problem. We set  $\mathbf{V} = [U, W]^T$  and denote by  $\hat{\mathbf{F}}_\rho^\mathcal{L}$ ,  $\hat{\mathcal{F}}_\mathbf{V}^\mathcal{L}$  and  $\hat{\mathbf{F}}_E^\mathcal{L}$  the rows in  $\hat{\mathcal{F}}^\mathcal{L}$  corresponding to density, momentum and energy, respectively. Under these assumptions, the linear problem arising from the SI-DG formulation reads:

find  $(\rho_{tt}, \mathbf{V}_{tt}, E_{tt}, p_{tt}) \in V_h \times (V_h)^2 \times V_h \times V_h$  such that  $\forall K \in \mathcal{T}_h, I = 1, \dots, \mathcal{N}$ :

$$\begin{aligned}
& \int_K \rho_{tt} \Phi_I \, d\mathbf{x} - \alpha \int_K \mathbf{V}_{tt} \cdot \nabla \Phi_I \, d\mathbf{x} + \alpha \int_{\partial K} \hat{\mathbf{F}}_\rho^\mathcal{L} \cdot \mathbf{n}_{\partial K} \Phi_I \, d\sigma = \int_K \rho^* \Phi_I \, d\mathbf{x} \\
& \int_K \mathbf{V}_{tt} \Phi_I \, d\mathbf{x} - \alpha \int_K p_{tt} \mathcal{I} \cdot \nabla \Phi_I \, d\mathbf{x} + \alpha \int_{\partial K} \hat{\mathcal{F}}_\mathbf{V}^\mathcal{L} \cdot \mathbf{n}_{\partial K} \Phi_I \, d\sigma = \int_K \mathbf{V}^* \Phi_I \, d\mathbf{x} \\
& \int_K E_{tt} \Phi_I \, d\mathbf{x} - \alpha \int_K \bar{h} \mathbf{V}_{tt} \cdot \nabla \Phi_I \, d\mathbf{x} + \alpha \int_{\partial K} \hat{\mathbf{F}}_E^\mathcal{L} \cdot \mathbf{n}_{\partial K} \Phi_I \, d\sigma = \int_K E^* \Phi_I \, d\mathbf{x} \\
& \int_K p_{tt} \Phi_I \, d\mathbf{x} = \frac{R}{c_v} \int_K E_{tt} \Phi_I \, d\mathbf{x}
\end{aligned} \tag{5.1}$$

with  $\alpha = \rho_{-1} \gamma \Delta t$ . Equations (5.1)<sub>2,3,4</sub> then immediately provide the problem:

find  $(p_{tt}, \mathbf{V}_{tt}) \in V_h \times (V_h)^2$  such that  $\forall K \in \mathcal{T}_h, I = 1, \dots, \mathcal{N}$

$$\begin{aligned} \int_K p_{tt} \Phi_I \, d\mathbf{x} - \alpha \frac{R}{c_v} \int_K \bar{h} \mathbf{V}_{tt} \cdot \nabla \Phi_I \, d\mathbf{x} + \alpha \frac{R}{c_v} \int_{\partial K} \bar{h} \hat{\mathbf{V}} \cdot \mathbf{n}_{\partial K} \Phi_I \, d\sigma &= \int_K p^* \Phi_I \, d\mathbf{x} \\ \int_K \mathbf{V}_{tt} \cdot \Phi_I \, d\mathbf{x} - \alpha \int_K p_{tt} \nabla \cdot \Phi_I \, d\mathbf{x} + \alpha \int_{\partial K} (\hat{p} \mathbf{n}_{\partial K}) \cdot \Phi_I \, d\sigma &= \int_K \mathbf{V}^* \cdot \Phi_I \, d\mathbf{x} \end{aligned} \quad (5.2)$$

where  $\Phi_I = [\Phi_I, 0]^T$  or  $\Phi_I = [0, \Phi_I]^T$ ,  $p^* = \frac{R}{c_v} E^*$  and the numerical fluxes are

$$\hat{\mathbf{V}} = \{\mathbf{V}_{tt}\} + \frac{|\bar{\lambda}|}{2} \frac{c_v}{R\bar{h}_h} \llbracket p_{tt} \rrbracket, \quad \hat{p} = \{p_{tt}\} \mathcal{I} + \frac{|\bar{\lambda}|}{2} \llbracket \mathbf{V}_{tt} \rrbracket. \quad (5.3)$$

Problem (5.2) can be fully regarded as the LDG discretization of the following elliptic problem for the sole pressure variable (see Eq. (2.2) and (2.3) in [13])

$$-\alpha^2 \nabla \cdot (\bar{a}^2 \nabla p_{tt}) + p_{tt} = -\alpha \nabla \cdot (\bar{a}^2 \mathbf{V}^*) + p^* \quad (5.4)$$

supplied with numerical fluxes (5.3), except for the fact that  $\llbracket \mathbf{V}_{tt} \rrbracket$  is used in (5.3)<sub>2</sub> instead of  $\llbracket \mathbf{V}_{tt} \rrbracket$ .

REMARK 5.1. *The elliptic numerical fluxes (5.3) descend from the hyperbolic numerical flux (4.6). In particular, the dissipative term  $\frac{|\bar{\lambda}|}{2} \llbracket \mathbf{q}_h \rrbracket$  in this latter flux gives rise to the two stabilization terms in (5.3).*

As discussed in [13], the inclusion of the jump term in (5.3)<sub>2</sub> makes it impossible to compute  $\mathbf{V}_{tt}$  *element by element* in terms of  $p_{tt}$  from (5.2)<sub>2</sub>. This implies that, starting from (5.2), it is not possible to obtain in an efficient way a discrete counterpart of (5.4) involving the sole pressure variable. However, we show now how, by taking advantage of the approximate quadrature rule, it is possible to compute  $\mathbf{V}_{tt}$  *node by node* in terms of  $p_{tt}$ . To this end, we need to work out the matrix formulation of (5.2), and some additional notation is required. We denote by  $\mathcal{M}$  the number of quadrature nodes in  $\mathcal{T}_h$ , and we assume without loss of generality that the first  $\mathcal{M}^\varepsilon$  of such nodes are located on  $\mathcal{E}_h$ . For the  $Q$ -th quadrature node, we denote by  $I_q(Q)$  the degrees of freedom collocated at the quadrature node itself, with  $q = 1, \dots, n_Q$ . For  $Q > \mathcal{M}^\varepsilon$  we have  $n_Q = 1$ ; for  $Q \leq \mathcal{M}^\varepsilon$ , on the one hand we have  $n_Q \geq 2$  thanks to the periodic boundary conditions and, on the other hand, the regularity of  $\mathcal{T}_h$  implies an upper bound for  $n_Q$ . Symmetrically, for a degree of freedom  $I$  we denote by  $Q(I)$  the corresponding quadrature node. Notice that, for a continuous function  $\chi$ , we have  $\chi_{I_{q_1}(Q)} = \chi_{I_{q_2}(Q)} = \chi_Q$ . For a given pair  $(Q, e)$ , with  $Q$  collocated on  $e$ , we use the shorthand notation  $I_{Q,e}, I'_{Q,e}$  to indicate two degrees of freedom such that  $I_{Q,e} \neq I'_{Q,e}$ ,  $Q(I_{Q,e}) = Q(I'_{Q,e})$  and  $I_{Q,e}$  and  $I'_{Q,e}$  belong to a couple of elements  $K, K'$  such that  $\partial K \cap \partial K' = e$ . Notice that the subscript  $(Q, e)$  will be usually omitted, since it is clear from the context. Finally, for  $I = (K, ij)$  we denote by  $\mathcal{E}_I$  the set of edges  $e$  such that  $e \in \partial K$  and  $Q(I)$  is collocated on  $e$ .

The integrals on the interior of  $K$  can be easily expressed in terms of the  $\mathcal{N} \times \mathcal{N}$  matrices  $M, D_x$  and  $D_z$  defined respectively in (4.9) and by

$$(D_x)_{IJ} = - \int_K \frac{\partial \Phi_I}{\partial x} \Phi_J \, d\mathbf{x}, \quad (D_z)_{IJ} = - \int_K \frac{\partial \Phi_I}{\partial z} \Phi_J \, d\mathbf{x}, \quad (5.5)$$

which, due to the discontinuous nature of the basis functions, are block-diagonal. Concerning the boundary integrals, we illustrate the treatment of (5.2)<sub>1</sub>, as analogous

considerations apply to (5.2)<sub>2</sub>. Dropping the subscript  $tt$  for simplicity, we have

$$\begin{aligned} & \int_{\partial K} \frac{R}{c_v} \bar{h} \hat{\mathbf{V}} \cdot \mathbf{n}_{\partial K} \Phi_I \, d\sigma \\ &= \sum_{e \in \mathcal{E}_I} \omega_I^e \left\{ \frac{|\bar{\lambda}_I|}{2} (p_I - p_{I'}) + \frac{1}{2} \frac{R \bar{h}_I}{c_v} [(U_I + U_{I'}) n_x + (W_I + W_{I'}) n_z] \right\} \\ &= \frac{|\bar{\lambda}_{Q(I)}|}{2} \sum_{e \in \mathcal{E}_I} \omega_I^e (p_I - p_{I'}) + \frac{1}{2} \frac{R \bar{h}_{Q(I)}}{c_v} \sum_{e \in \mathcal{E}_I} \omega_I^e [(U_I + U_{I'}) n_x + (W_I + W_{I'}) n_z]. \end{aligned}$$

Let now  $D^s$ ,  $BN_x$  and  $BN_z$  denote the  $\mathcal{N} \times \mathcal{N}$  matrices such that

$$(D^s q_h)_I = \frac{1}{2} \sum_{e \in \mathcal{E}_I} \omega_I^e (q_I - q_{I'}), \quad (BN_{x,z} q_h)_I = \frac{1}{2} \sum_{e \in \mathcal{E}_I} \omega_I^e (q_I + q_{I'}) n_{x,z}$$

with  $q_h$  denoting either  $p_h$ ,  $U_h$  or  $W_h$ . It is easy to verify that, up to a permutation of the unknowns,  $D^s$ ,  $BN_x$  and  $BN_z$  have a block diagonal structure with  $\mathcal{M}^\mathcal{E}$  non-zero blocks of dimension  $n_Q$ ,  $Q = 1, \dots, \mathcal{M}^\mathcal{E}$ , respectively. In particular, for the case of a quadrature node belonging to one sole edge  $e$  (i.e., not corner point), we have  $n_Q = 2$  and the  $2 \times 2$  blocks

$$D_Q^s = \frac{1}{2} \begin{bmatrix} 1 & -1 \\ -1 & 1 \end{bmatrix} \omega_Q^e,$$

and

$$BN_{x_Q} = \frac{1}{2} \begin{bmatrix} n_{x_e, I_1(Q)} & n_{x_e, I_1(Q)} \\ n_{x_e, I_2(Q)} & n_{x_e, I_2(Q)} \end{bmatrix} \omega_Q^e, \quad BN_{z_Q} = \frac{1}{2} \begin{bmatrix} n_{z_e, I_1(Q)} & n_{z_e, I_1(Q)} \\ n_{z_e, I_2(Q)} & n_{z_e, I_2(Q)} \end{bmatrix} \omega_Q^e,$$

with  $\omega_Q^e = \omega_{I_{Q,e}}^e = \omega_{I'_{Q,e}}^e$ .

Summarizing, the matrix counterpart of (5.2) after proper use of numerical integration reads:

$$\begin{cases} (M + \alpha \Lambda D^s) p + \alpha [(D_x + BN_x) A U + (D_z + BN_z) A W] = M p^* \\ (M + \alpha \Lambda D^s) U + \alpha (D_x + BN_x) p = M U^* \\ (M + \alpha \Lambda D^s) W + \alpha (D_z + BN_z) p = M W^* \end{cases} \quad (5.6)$$

where  $\Lambda$  and  $A$  are  $\mathcal{N} \times \mathcal{N}$  diagonal matrices defined as

$$\Lambda_{IJ} = |\bar{\lambda}_{Q(I)}| \delta_{IJ}, \quad A_{IJ} = \frac{R}{c_v} \bar{h}_{Q(I)} \delta_{IJ}.$$

The key element for the reformulation of (5.6) in terms of the sole unknown  $p$  relies on an efficient computation of the inverse of the matrix  $M^{DG} = M + \alpha \Lambda D^s$ . We have

$$(M^{DG})^{-1} = (I + \alpha \Lambda M^{-1} D^s)^{-1} M^{-1} := \Sigma M^{-1}.$$

Since  $\Sigma^{-1} = (I + \alpha \Lambda M^{-1} D^s)$ , it turns out that  $\Sigma$  has the same block diagonal structure as  $D^s$ , so that its computation is straightforward (see Fig. 5.1).

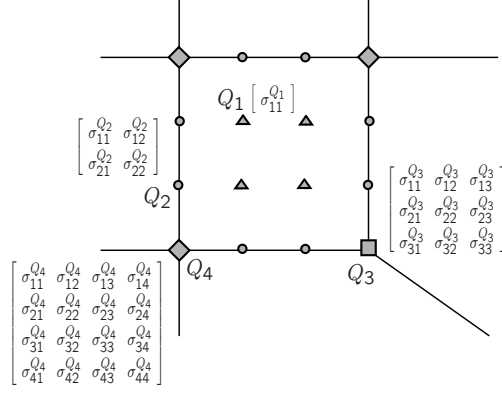


FIGURE 5.1. Representation of the block diagonal structure of the matrix  $\Sigma$ . A  $1 \times 1$  block is associated with internal quadrature nodes ( $\triangle$ ) such as  $Q_1$ , and we have  $\sigma_{11}^{Q_1} = 1$ . Quadrature nodes belonging to one sole edge ( $\circ$ ), such as  $Q_2$ , give rise to  $2 \times 2$  blocks. Finally, nodes belonging to two or more edges ( $\square$  and  $\diamond$ ), such as  $Q_3$  and  $Q_4$ , give rise to  $n_Q \times n_Q$  blocks.

Upon defining  $\tilde{D}_x^{DG} = (M^{DG})^{-1} (D_x + BN_x)$ ,  $\tilde{D}_z^{DG} = (M^{DG})^{-1} (D_z + BN_z)$ ,  $\tilde{p} = \Sigma p^*$ ,  $\tilde{U} = \Sigma U^*$  and  $\tilde{W} = \Sigma W^*$ , system (5.6) can be written as

$$\begin{cases} p + \alpha [\tilde{D}_x^{DG} A U + \tilde{D}_z^{DG} A W] = \tilde{p} \\ U + \alpha \tilde{D}_x^{DG} p = \tilde{U} \\ W + \alpha \tilde{D}_z^{DG} p = \tilde{W}. \end{cases} \quad (5.7)$$

Substituting (5.7)<sub>2,3</sub> into (5.7)<sub>1</sub> we obtain

$$p - \alpha^2 (\tilde{D}_x^{DG} A \tilde{D}_x^{DG} + \tilde{D}_z^{DG} A \tilde{D}_z^{DG}) p = \tilde{p} - \alpha (\tilde{D}_x^{DG} A \tilde{U} + \tilde{D}_z^{DG} A \tilde{W}). \quad (5.8)$$

Problem (5.8) is the discrete counterpart of (5.4). The advantages of solving (5.8) instead of (5.6) will be numerically demonstrated in § 6.2.

**6. Numerical Results.** In this section, the numerical validation of the proposed scheme is carried out. To simplify the presentation, rather than giving a detailed description of each test case setup, we provide references to some classical works in the literature. In addition, a comprehensive overview of all the test cases can be found in [29]. For ease of comparison with the literature, all the results are converted to primitive variables:  $\pi$  is the Exner pressure,  $u$  and  $w$  are the horizontal and vertical velocities, respectively, and  $\theta$  is the potential temperature. Deviations from the background atmosphere, which is characterized by a uniform Brunt–Väisälä frequency  $N = \frac{g}{\theta} \frac{d\theta}{dz}$  (see [22]), are displayed. Following [44], the reference state  $\bar{\mathbf{q}}$  (see § 2) is isothermal in all the test cases, with  $\bar{T}$  being the highest temperature in the initial condition. The local Courant number and advective Courant number are defined as  $C = \frac{a \Delta t}{h_{LGL}}$  and  $C_{adv} = \frac{v \Delta t}{h_{LGL}}$ , respectively, where  $h_{LGL}$  denotes the (variable) spacing between the Legendre–Gauss–Lobatto points (see § 4.2). The maximum values of  $C$  and  $C_{adv}$  in the domain are denoted by  $C^{max}$  and  $C_{adv}^{max}$ , respectively. All the computations described in this section employ the BDF2 scheme of Tab. 3.1; notice however that similar results are obtained with the TM and LF2 schemes. To compare our results with other results in the literature, it is convenient, for a given grid of

high-order elements, to define the equivalent resolution as the resolution of a uniform grid with the same number  $\mathcal{M}$  of grid points. Finally, for the mountain waves test cases the Root-Mean-Square (RMS) errors are computed as in [29].

**6.1. Inertia-Gravity Waves.** In this section, we study the nonhydrostatic inertia-gravity wave test proposed in [45]. A background atmosphere is considered with constant Brunt–Väisälä frequency  $N = 0.01 \text{ s}^{-1}$  and uniform horizontal flow  $\bar{u} = 20 \text{ m/s}$ . The computational domain is  $[0 \text{ km}, 300 \text{ km}] \times [0 \text{ km}, 10 \text{ km}]$ , with no-flux boundary conditions on bottom and top boundaries and periodic conditions on lateral boundaries. The flow is inviscid. The initial condition is represented by a thermal anomaly centered at  $(x, z) = (100 \text{ km}, 5 \text{ km})$ , and the flow is simulated until  $T_{fin} = 3000 \text{ s}$ . A grid composed by  $120 \times 4$ , 10<sup>th</sup>-order elements is employed, with equivalent resolution  $0.25 \text{ km}$ . The time-step is  $1 \text{ s}$ , yielding  $C^{max} = 5.1$  and  $C_{adv}^{max} = 0.24$ . The computed potential temperature  $\theta$  is shown in Fig. 6.1. These results are in good agreement with those presented in [45, 1, 29]. To assess in greater details the effect of the semi-implicit time discretization, in Fig. 6.1, right, the computed profile from [29] with explicit time stepping is also reported. It can be seen that the two curves are nearly coincident. Extrema for the computed solution are  $(-7.128 \cdot 10^{-7}, 9.106 \cdot 10^{-7})$  for  $\pi$ ,  $(-1.061 \cdot 10^{-2} \text{ m/s}, 1.064 \cdot 10^{-2} \text{ m/s})$  for  $u$ ,  $(-2.402 \cdot 10^{-3} \text{ m/s}, 2.877 \cdot 10^{-3} \text{ m/s})$  for  $w$  and  $(-1.511 \cdot 10^{-3} \text{ K}, 2.806 \cdot 10^{-3} \text{ K})$  for  $\theta$ . The corresponding relative differences with respect to the explicit case are 46.9%, 0.56%, 13.4% and 0.68%, respectively, thus confirming that the distortion caused by the semi-implicit time discretization for acoustic modes, which is evident in the large pressure difference, does not affect the slow modes. Finally, concerning conservation, we notice that for this problem we expect mass, horizontal momentum and total energy to remain constant. This is verified up to machine precision in the numerical simulation, where we observe for these three quantities relative errors equal to  $1.669 \cdot 10^{-8}$ ,  $2.645 \cdot 10^{-7}$  and  $1.640 \cdot 10^{-8}$ , respectively.

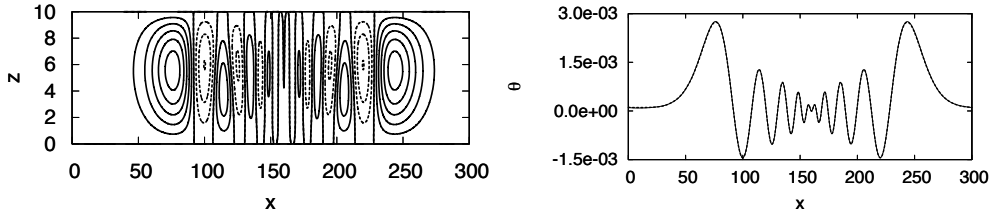


FIGURE 6.1. Inertia-gravity wave test case, potential temperature at time level 3000 s (coordinates in km). Left: contour plot with contour values between  $-1.5 \cdot 10^{-3} \text{ K}$  and  $3 \cdot 10^{-3} \text{ K}$  with contour interval  $5 \cdot 10^{-4} \text{ K}$  (negative values: dashed lines). Right: profile along 5 km height for the semi-implicit (continuous) and for the explicit (dashed) DG formulations.

**6.2. Bubble Convection Experiments.** In this section, we study four idealized test cases characterized by buoyancy driven flows. In these tests, a basic-state atmosphere is considered, which is assumed to be at rest and in hydrostatic equilibrium, and a thermal anomaly, with a consequent density perturbation, is introduced.

The first test case is similar to the smooth bubble test proposed in [12, 40]. The basic state atmosphere is characterized by neutral stratification, and the flow is driven by a smooth thermal anomaly of which the maximum amplitude is  $+0.5 \text{ K}$ . Reflecting boundary conditions are applied and the flow is inviscid. The computational domain is  $[0 \text{ m}, 1000 \text{ m}] \times [0 \text{ m}, 1000 \text{ m}]$  and a grid composed of  $20 \times 20$ ,



10<sup>th</sup>-order elements is adopted, with equivalent resolution  $5m$ . The time step is  $0.08s$ , yielding  $C^{max} = 19$  and  $C_{adv}^{max} = 0.12$ . Figure 6.2 shows the computed potential temperature perturbation at  $T_{fin} = 600s$  and the one-dimensional profile along  $z = 700m$  for the same quantity. Minimum and maximum values for the computed solution are  $(-1.125 \cdot 10^{-5}, 5.016 \cdot 10^{-6})$  for  $\pi$ ,  $(-2.161 m/s, 2.161 m/s)$  for  $u$ ,  $(-1.967 m/s, 2.758 m/s)$  for  $w$  and  $(-7.303 \cdot 10^{-2} K, 5.259 \cdot 10^{-1} K)$  for  $\theta$ . All these results are in good agreement with those reported in [29] for the explicit case. Concerning conservation, for this problem we expect mass and total energy to remain constant. This is verified up to machine precision in the numerical simulation, where we observe for these quantities relative deviations equal to  $8.755 \cdot 10^{-11}$  and  $4.627 \cdot 10^{-11}$ , respectively.

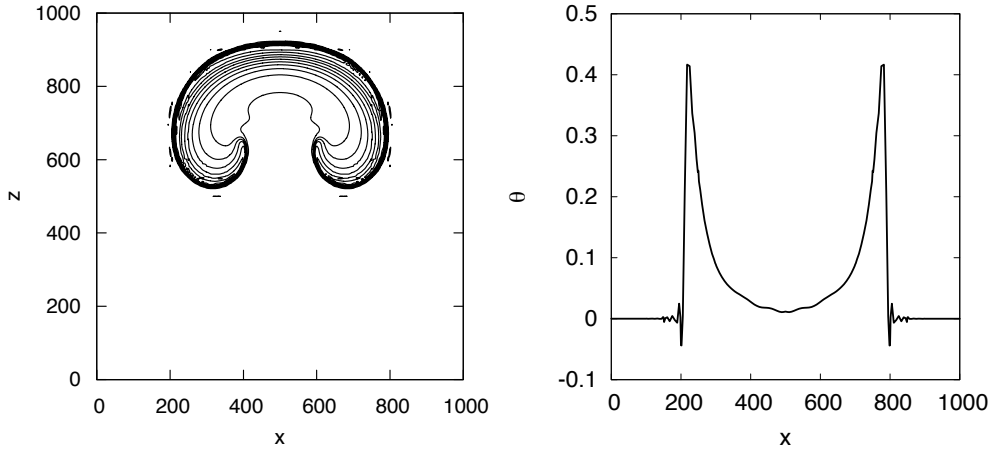


FIGURE 6.2. *Smooth bubble test case, potential temperature perturbation at time level 600 s. Left: contour plot using values between  $0.025 K$  and  $0.525 K$  with an interval of  $0.05 K$ . Right: profile along constant height  $z = 700 m$ .*

The second test case is analogous to the first one, except that a non-smooth thermal anomaly is considered and the computational domain is larger. A very similar test case was also proposed in [40]. To deal with the non-smooth initial datum, a viscosity  $\nu = 0.4 m^2/s$  is introduced, and we assume  $Pr = 1$ . Reflecting boundary conditions are applied, except for the energy balance equation, where the temperature gradient is imposed on bottom and top boundaries to avoid the formation of a thermal boundary layer, as discussed in [29]. The computational domain is  $[0m, 1000m] \times [0m, 1500m]$  and a grid composed of  $20 \times 30$ , 10<sup>th</sup>-order elements is adopted, with equivalent resolution  $5m$ . The time step is  $0.08s$ , yielding  $C^{max} = 19$  and  $C_{adv}^{max} = 0.15$ . Figure 6.3 shows the computed potential temperature perturbation after  $600s$  and the one-dimensional profile along  $z = 1000m$  for the same quantity. Minimum and maximum values for the computed solution are  $(-2.563 \cdot 10^{-5}, 1.418 \cdot 10^{-5})$  for  $\pi$ ,  $(-2.386 m/s, 2.386 m/s)$  for  $u$ ,  $(-3.965 m/s, 2.450 m/s)$  for  $w$  and  $(-1.370 \cdot 10^{-3} K, 5.026 \cdot 10^{-1} K)$  for  $\theta$ . All these results are in good agreement with those reported in [29] for the explicit case. Concerning conservation, for this problem we expect mass to remain constant. This is verified up to machine precision in the numerical simulation, where we observe a relative deviation of  $2.555 \cdot 10^{-11}$ .

The third test case is the density current test proposed in [47], consisting in a cold bubble placed in a neutral atmosphere. The bubble sinks until hitting the bottom

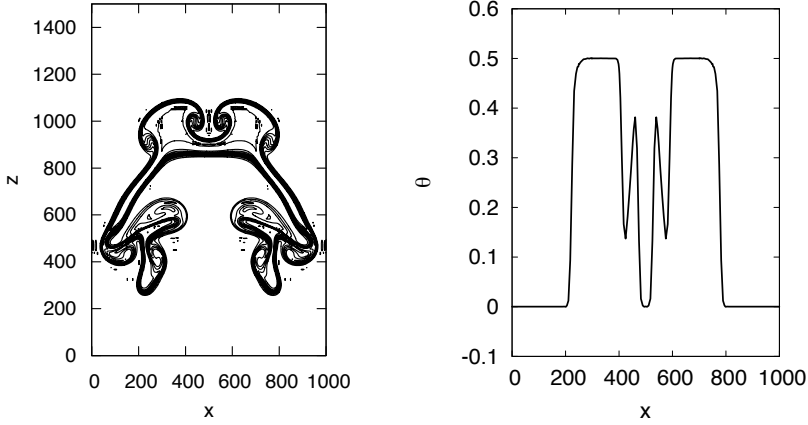


FIGURE 6.3. *Non-smooth bubble test case, potential temperature perturbation at time level 600 s. Left: contour plot using values between 0 K and 0.52 K with an interval of 0.05 K. Right: profile along constant height  $z = 1000 m$ .*

boundary, where no-flux conditions are imposed, and subsequently Kelvin–Helmholtz rotors develop. Viscosity is prescribed in such a way that a grid-converged solution can be obtained at approximately  $50 m$  resolution. Figure 6.4 shows the computed solution on two grids composed by  $8 \times 2$  and  $32 \times 8$ , 8<sup>th</sup>-order elements, respectively, with equivalent resolution  $400 m$  and  $100 m$ . Notice that, thanks to the symmetry of the problem, the solution is computed only in half of the domain. The time steps are  $0.8 s$  and  $0.2 s$ , respectively, with  $C^{max} = 2.1$  and  $C_{adv}^{max} = 0.18$ . The first case is representative of a poorly resolved flow, since the resolution is too coarse to capture all the features of the grid-converged solution, while the second case is representative of a well resolved flow. By comparing the results in Fig. 6.4 with those in [47], it can be seen that, on the one hand, in the poorly resolved case one of the three rolls present in the reference solution is clearly reproduced, yielding a result which is comparable to the low order *Monotonic Upstream Method* (MUPL) and *Piecewise Parabolic Method* (PPM) solutions. This is significant because, on the contrary, the high-order *Fully Local Spectral* (FLS) method produces in this case completely meaningless results. On the other hand, in the well resolved case the solution obtained with the SI-DG formulation is similar to the one obtained with the FLS and close to the grid-converged solution, being thus superior to those obtained with the MUPL and PPM schemes. Concerning conservation, we observe a mass relative difference of  $4.600 \times 10^{-12}$  and  $1.818 \times 10^{-11}$  in the coarse and fine resolution cases, respectively.

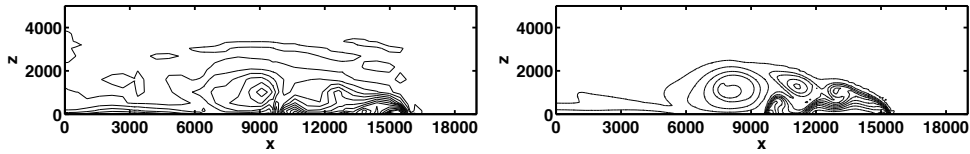


FIGURE 6.4. *Density current test case, potential temperature perturbation at time level 900 s using 400 m (left) and 100 m (right) resolution. Contour intervals are 1 K, with values between 0 K and  $-10 K$ , as in [47].*

The fourth test case aims at verifying the practical advantages of employing the

static condensation procedure illustrated in § 5.2. We thus set periodic boundary conditions on all the domain boundaries and we treat implicitly only the terms associated with acoustic waves. The computational domain is the rectangle  $[0\text{ m}, 1000\text{ m}] \times [0\text{ m}, 2000\text{ m}]$ , and the initial datum is represented by a thermal anomaly introduced in an isothermal atmosphere at  $T = 303\text{ K}$  (notice that, thanks to this choice, the deviations from the reference atmosphere are zero far from the thermal anomaly, which allows to enforce periodic boundary conditions on top and bottom boundaries). The thermal anomaly has amplitude  $-15\text{ K}$  and has the same profile as in the first bubble convection test case. Viscosity is set equal to  $0.2\text{ m}^2/\text{s}$ . The computational grid is composed by  $25 \times 50$ ,  $10^{\text{th}}$ -order elements, with equivalent resolution  $4\text{ m}$ , while the time-step  $0.02\text{ s}$ , yielding  $C^{\text{max}} = 6.1$  and  $C_{\text{adv}}^{\text{max}} = 0.15$ . The computed potential temperature is displayed in Fig. 6.5. A comparison between the solutions computed with and without performing the static condensation shows that the number of GMRES iterations required for the solution of the linear system decreases by approximately a factor 3 (from 45 to 15 iterations), while a rough comparison with the explicit time integration indicates a reduction in the overall computational time of approximately a factor 5. Here, we point out that these efficiency considerations need further verification on a wider set of test cases; nevertheless, the greater efficiency of the SIDG with mass lumping and static condensation seems to be out of question.

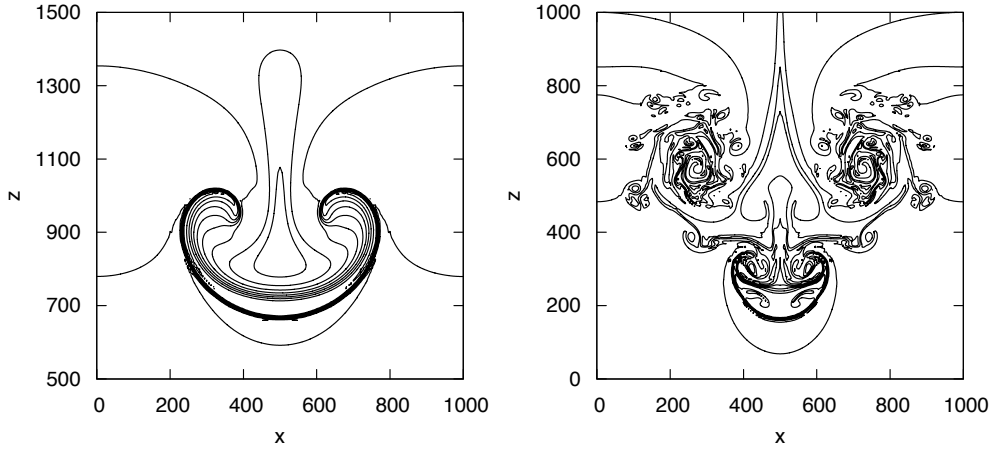


FIGURE 6.5. Cold bubble test case, potential temperature perturbation at time levels  $100\text{ s}$  (left) and  $200\text{ s}$  (right). Contour plots using values between  $-11.5\text{ K}$  and  $8\text{ K}$  with an interval of  $1.625\text{ K}$ .

**6.3. Mountain Wave Simulation.** In this section, we study three test cases based on the simulation of hydrostatic and nonhydrostatic mountain waves. Besides assessing the overall accuracy of the proposed numerical scheme, we intend with these tests to verify the robustness of the approach discussed in § 2.1 and § 3 to deal with open-boundary conditions in the framework of conservative formulation for the flow equations and semi-implicit time integration. All the test cases consider a uniform horizontal flow impinging over an isolated mountain. The background atmosphere is characterized by constant Brunt–Väisälä frequency; no flux conditions are imposed on the bottom boundary while open-boundary conditions are imposed on lateral and top boundaries. The flow is inviscid in all the test cases. A classical review on mountain waves is [46], while we refer to [32, 23, 36, 7, 42, 24, 25] for a detailed description of the test cases and reference solutions.

For the first test case, we consider an isothermal atmosphere at  $\bar{T} = 250, K$  and Brunt–Väisälä frequency  $N = 1.95 \cdot 10^{-2} s^{-1}$  and a uniform horizontal flow at  $\bar{u} = 20 m/s$ . The computational domain is  $[0 km, 240 km] \times [0 km, 30 km]$ , and the mountain profile is defined by the *versiera di Agnesi*

$$h_m(x) = \frac{h_{m_0}}{1 + \left(\frac{x-x_c}{a_c}\right)^2}, \quad (6.1)$$

with  $h_{m_0} = 1 m$ ,  $x_c = 120 km$  and  $a_c = 10 km$ . As shown in [46], this choice of parameters results in an hydrostatic flow. A grid composed by  $20 \times 12$ ,  $10^{th}$ -order elements is adopted, with equivalent resolution  $1.2 km$  in the horizontal and  $0.25 km$  in the vertical. The time-step is  $3.5 s$ , yielding  $C^{max} = 18.6$  and  $C_{adv}^{max} = 0.18$ . The computed solution at time level  $T_{fin} = 10 hrs.$  is represented in Fig. 6.6. A pseudo-analytic solution computed with Fourier transform techniques is also represented. In addition, figure 6.8, left, shows the computed vertical flux of horizontal momentum (whose magnitude equals the drag exerted by the flow on the obstacle), at various time levels, normalized by the analytic value

$$M_H = -\frac{\pi_c}{4} \bar{\rho}_s \bar{u} N h_{m_0}^2, \quad (6.2)$$

with  $\bar{\rho}_s = \bar{\rho}(0)$  denoting the surface density. In general, an overall agreement of the computed solution with the analytic solution can be observed. The RMS errors are  $1.44 \times 10^{-7}$  for  $\pi$ ,  $2.61 \times 10^{-3} m/s$  for  $u$ ,  $7.44 \times 10^{-5} m/s$  for  $w$  and  $1.79 \times 10^{-3} K$  for  $\theta$ . Concerning the normalized momentum flux, its value is close to 1 far from the upper boundary, and goes to zero within the damping layer. This fact is in good agreement with the analytic results and also confirms that a steady state configuration, characterized by a uniform momentum flux, is attained.

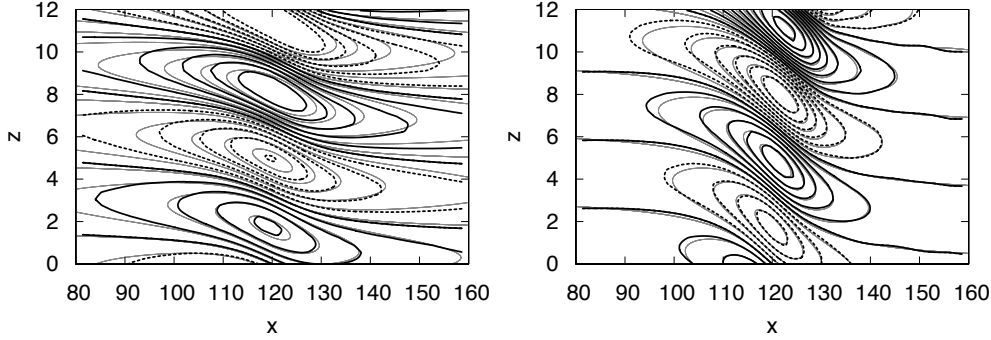


FIGURE 6.6. *Linear hydrostatic mountain test case, computed solution at time level 10 hrs. (black, dashed line for negative values) and analytic steady state solution (gray), coordinates in km. Left: horizontal velocity  $u$  with contour lines between  $-2.5 \cdot 10^{-2} m/s$  and  $2.5 \cdot 10^{-2} m/s$  with contour interval  $5 \cdot 10^{-3} m/s$ . Right: vertical velocity  $w$  with contour lines between  $-5 \cdot 10^{-3} m/s$  and  $5 \cdot 10^{-3} m/s$  with contour interval  $5 \cdot 10^{-4} m/s$ .*

For the second test case, we consider a constant stability atmosphere with Brunt–Väisälä frequency  $N = 1 \cdot 10^{-2} s^{-1}$  and surface temperature  $\bar{T}_s = 280 K$  and a uniform horizontal flow with  $\bar{u} = 10 m/s$ . The computational domain is  $[0 km, 144 km] \times [0 km, 30 km]$ , and the mountain profile is given by (6.1) with  $h_{m_0} = 1 m$ ,  $x_c = 72 km$  and  $a_c = 1 km$ . This choice of parameters results in a nonhydrostatic flow. A

grid composed by  $40 \times 10$ ,  $10^{\text{th}}$ -order elements is adopted, with equivalent resolution  $0.36 \text{ km}$  in the horizontal and  $0.3 \text{ km}$  in the vertical. The time-step is  $2 \text{ s}$ , yielding  $C^{\text{max}} = 8.39$  and  $C^{\text{max}}_{\text{adv}} = 0.17$ . The computed solution at time level  $T_{\text{fin}} = 5 \text{ hrs.}$  is represented in Fig. 6.7, together with a pseudo-analytic solution computed. Figure 6.8, right, shows the computed vertical flux of horizontal momentum at various intermediate time levels, normalized by the analytic value

$$M_{NH} = -0.457 \frac{\pi_c}{4} \bar{\rho}_s \bar{u} N h_{m_0}^2,$$

In general, an overall agreement of the computed solution with the analytic solution can be observed, although some incorrect maxima can be observed downstream the obstacle, which can be possibly ascribed to unphysical reflections in the absorbing layer. The RMS errors are  $2.28 \times 10^{-8}$  for  $\pi$ ,  $6.98 \times 10^{-4} \text{ m/s}$  for  $u$ ,  $2.59 \times 10^{-4} \text{ m/s}$  for  $w$  and  $2.50 \times 10^{-4} \text{ K}$  for  $\theta$ . Concerning the normalized momentum flux, the same considerations as for the previous case apply.

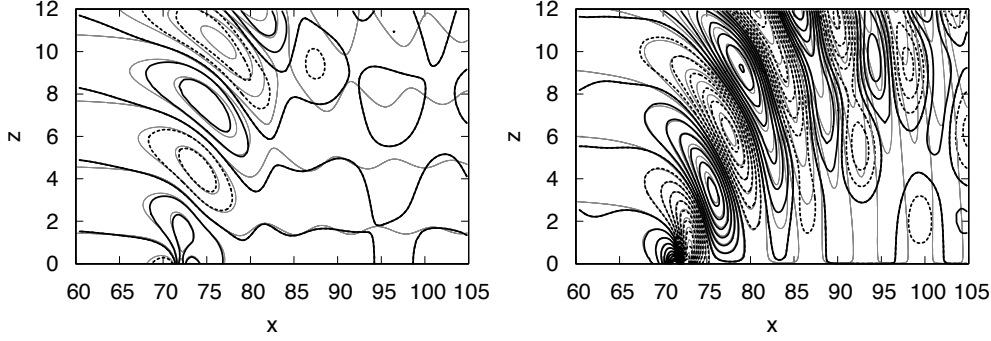


FIGURE 6.7. Linear nonhydrostatic mountain test case, computed solution at time level 5 hrs. (black, dashed line for negative values) and analytic steady state solution (gray), coordinates in km. Left: horizontal velocity  $u$  with contour lines between  $-2.5 \cdot 10^{-2} \text{ m/s}$  and  $2.5 \cdot 10^{-2} \text{ m/s}$  with contour interval  $2.5 \cdot 10^{-3} \text{ m/s}$ . Right: vertical velocity  $w$  with contour lines between  $-5 \cdot 10^{-3} \text{ m/s}$  and  $5 \cdot 10^{-3} \text{ m/s}$  with contour interval  $5 \cdot 10^{-4} \text{ m/s}$ .

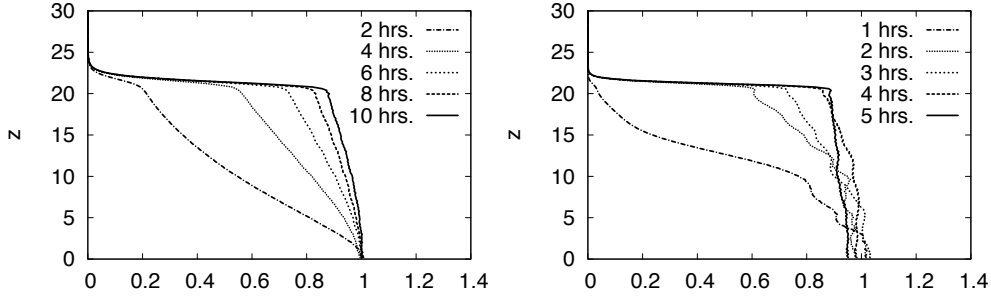


FIGURE 6.8. Mountain wave test cases, normalized vertical flux of horizontal momentum. Left: hydrostatic case, time levels 2 hrs., 4 hrs., 6 hrs., 8 hrs. and 10 hrs.. Right: nonhydrostatic case, time levels 1 hrs., 2 hrs., 3 hrs., 4 hrs. and 5 hrs..

The third test case has been proposed in [42], and various solutions are available in the literature, as for instance [24, 25]. A uniform stability background atmosphere is considered with Brunt–Väisälä frequency  $N = 1 \cdot 10^{-2} \text{ s}^{-1}$  and surface temperature

$\bar{T}_s = 280 K$  and a uniform horizontal flow with  $\bar{u} = 10 m/s$ . The computational domain is  $[-25 km, 25 km] \times [0 km, 21 km]$ , and the mountain profile is

$$h_m(x) = h_{m_0} e^{-\left(\frac{x}{a_c}\right)^2} \cos^2\left(\frac{\pi_c x}{\lambda_c}\right)$$

with  $h_{m_0} = 250 m$ ,  $a_c = 5 km$  and  $\lambda_c = 4 km$ . As pointed out in [42], the orography profile forces two distinct types of internal waves: a large-scale hydrostatic wave characterized by deep vertical propagation and a smaller-scale, nonhydrostatic wave characterized by rapid decay with height. A grid composed by  $20 \times 10$ , 10<sup>th</sup>-order elements is adopted, with equivalent resolution  $0.25 km$  in the horizontal and  $0.21 km$  in the vertical. The time-step is  $1.4 s$ , yielding  $C^{max} = 8.40$  and  $C_{adv}^{max} = 0.20$ . The computed solution at time level  $T_{fin} = 10 hrs.$  is represented in Fig. 6.9, together with a pseudo-analytic linear solution. Notice, however, that due to the non-negligible height of the mountain, the linear solution should be taken as a qualitative reference rather than “the” solution. A good agreement of the numerical solution is observed both with the analytic linear solution and with results in the literature. In particular, notice that the numerical solution correctly reproduces the different vertical structures of the two superimposed waves, with the small-scale perturbation exhibiting the correct decay with height. The RMS errors are  $7.93 \times 10^{-6}$  for  $\pi$ ,  $1.87 \times 10^{-1} m/s$  for  $u$ ,  $3.86 \times 10^{-2} m/s$  for  $w$  and  $4.41 \times 10^{-2} K$  for  $\theta$ . Figure 6.10 shows a detail of the computational grid, left, and the computed vertical flux of horizontal momentum at various intermediate time levels, normalized by the analytic value for the hydrostatic case (6.2), right. The momentum flux is constant along the vertical, indicating that a steady state configuration is reached, and a value different from one is explained by the different shape of the mountain with respect to the previous test.

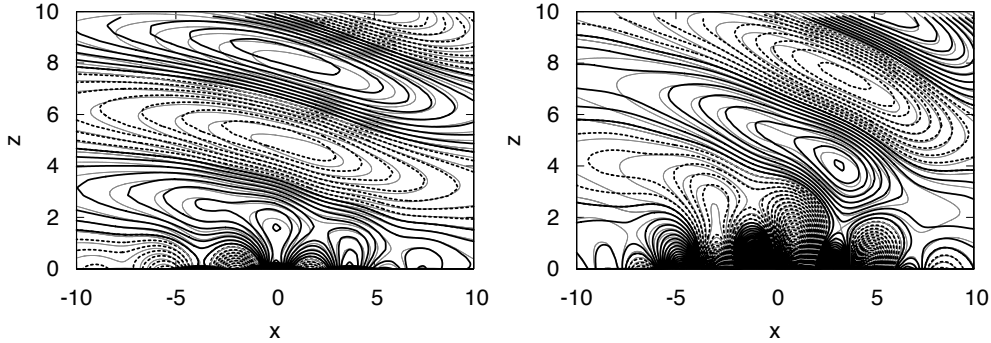


FIGURE 6.9. Schär mountain test case, computed solution at time level 10 hrs. (black, dashed line for negative values) and linearized analytic steady state solution (gray), coordinates in km. Left: horizontal velocity  $u$  with contour lines between  $-2 m/s$  and  $2 m/s$  with contour interval  $0.2 m/s$ . Right: vertical velocity  $w$  with contour lines between  $-2 m/s$  and  $2 m/s$  with contour interval  $0.05 m/s$ .

**7. Conclusions.** In the present article we have proposed a formulation in which the SI time integration strategy is adopted in the context of a high-order DG spatial discretization for the solution of the nonhydrostatic, compressible Navier–Stokes equation for atmospheric flows. The main reason for investigating this combination is the increase of the efficiency of the DG method when applied to mesoscale flows, and more in general to low Mach number compressible flows. A critical step in a SI

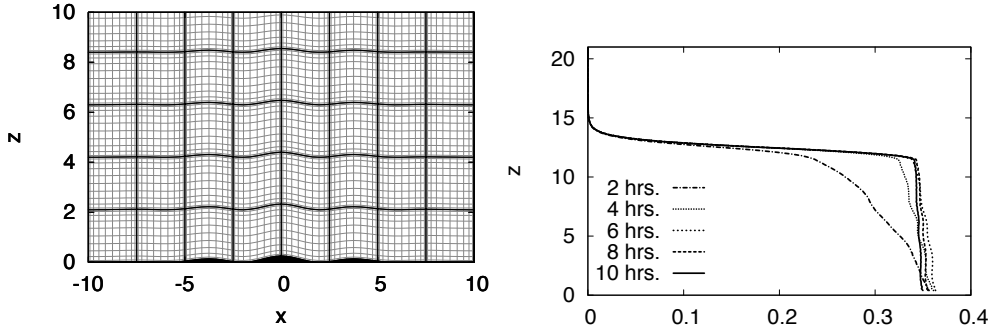


FIGURE 6.10. *Schär mountain test cases. Left: computational grid, element boundaries are displayed in black and LGL points are located at the intersections of the gray lines. Right: normalized vertical flux of horizontal momentum at time levels 2 hrs., 4 hrs., 6 hrs., 8 hrs. and 10 hrs..*

formulation is represented by the solution of the linear system for the implicit part of the scheme. We have shown that it is possible to reformulate such a problem in terms of a pseudo-Helmholtz operator, and that the resulting discretization fits into the LDG framework for elliptic problems. We have also indicated how it is possible to sidestep some well known difficulties in dealing with penalization terms in the numerical fluxes by exploiting the LGL numerical quadrature. The potential benefits of this approach have then been demonstrated with some classical numerical tests. In the future, we plan to implement the pseudo-Helmholtz form of the linear system for the case of general boundary conditions, explore alternative high-order non-reflective boundary conditions and extend the model to three dimensions to investigate the effects of rotation. A further possible extension is represented by the introduction of the semi-Lagrangian DG method proposed in [38] to deal with the stability limit associated with advection.

**Acknowledgements.** The work of the first author was mainly done while he was Ph.D. student at “Dipartimento di Matematica F. Brioschi, Politecnico di Milano”, under the supervision of [Riccardo Sacco](#) and [Luca Bonaventura](#), whom he wishes to thank for several discussions which greatly improved the present manuscript.

#### REFERENCES

- [1] N. AHMAD AND J. LINDEMAN, *Euler solutions using flux-based wave decomposition*, Int. J. Numer. Meth. Fl., 54 (2007), pp. 47–72.
- [2] V. AIZINGER AND C. DAWSON, *A discontinuous Galerkin method for two-dimensional flow and transport in shallow water*, Adv. Water Resour., 25 (2002), pp. 67–84.
- [3] D.N. ARNOLD AND F. BREZZI, *Mixed and nonconforming finite-element methods - implementation, postprocessing and error-estimates*, RAIRO - Math. Model. Num., 19 (1985), pp. 7–32.
- [4] D.N. ARNOLD, F. BREZZI, B. COCKBURN, AND L.D. MARINI, *Unified analysis of discontinuous Galerkin methods for elliptic problems*, SINUM, 39 (2002), pp. 1749–1779.
- [5] F. BASSI AND S. REBAY, *A high-order accurate discontinuous finite element method for the numerical solution of the compressible Navier–Stokes equations*, J. Comp. Phys., 131 (1997), pp. 267–279.
- [6] —, *High-order accurate discontinuous finite element solution of the 2D Euler Equations*, J. Comp. Phys., 138 (1997), pp. 251–285.
- [7] L. BONAVENTURA, *A semi-implicit semi-Lagrangian scheme using the height coordinate for a nonhydrostatic and fully elastic model of atmospheric flows*, J. Comp. Phys., 158 (2000), pp. 186–213.



- [8] N. BOTTA, R. KLEIN, S. LANGENBERG, AND S. LÜTZENKIRCHEN, *Well balanced finite volume methods for nearly hydrostatic flows*, J. Comp. Phys., 196 (2004), pp. 539–565.
- [9] J.P. BOYD, *Chebyshev and Fourier spectral methods*, Dover Publications Inc., Mineola, New York, 2001.
- [10] D.M. BURRIDGE, *A split semi-implicit reformulation of the Bushby–Timpson 10-level model*, Q. J. R. Meteorol. Soc., 101 (1975), pp. 777–792.
- [11] C. CANUTO, M.Y. HUSSAINI, A. QUARTERONI, AND T.A. ZANG, *Spectral Methods*, Springer, 2006.
- [12] R.L. CARPENTER, K.K. DROEGEMEIER, P.R. WOODWARD, AND C.E. HANE, *Application of the piecewise parabolic method (PPM) to meteorological modeling*, Mon. Wea. Rev., 118 (1990), pp. 586–612.
- [13] P. CASTILLO, B. COCKBURN, I. PERUGIA, AND D. SCHÖTZAU, *An a priori error analysis of the local discontinuous Galerkin method for elliptic problems.*, SINUM, 38 (2000), pp. 1676–1706.
- [14] B. COCKBURN, B. DONG, AND J. GUZMÁN, *A superconvergent LDG hybridizable Galerkin method for second order elliptic problems.*, Math. Comp., submitted (2007).
- [15] B. COCKBURN, B. DONG, J. GUZMÁN, M. RESTELLI, AND R. SACCO, *Superconvergent and optimally convergent hybridizable discontinuous Galerkin methods for convection-diffusion-reaction problems*, in preparation, (2007).
- [16] B. COCKBURN, C. JOHNSON, C.W. SHU, AND E. TADMOR, *Advanced Numerical Approximation of Nonlinear Hyperbolic Equations*, Springer, 1997.
- [17] B. COCKBURN AND C.W. SHU, *The local discontinuous Galerkin method for time-dependent convection-diffusion systems.*, SINUM, 35 (1998), pp. 2440–2463.
- [18] M. J. P. CULLEN, *A test of a semi-implicit integration technique for a fully compressible non-hydrostatic model*, Q. J. R. Meteorol. Soc., 116 (1990), pp. 1253–1258.
- [19] C. DAWSON AND V. AIZINGER, *A discontinuous Galerkin method for three-dimensional shallow water equations*, J. Sci. Comp., 22-23 (2005), pp. 245–267.
- [20] J. DEA, F.X. GIRALDO, AND B. NETA, *High-order Higdon non-reflecting boundary conditions for the linearized Euler equations*, NPS Technical Report NPS-MA-07-001, Naval Postgraduate School, Monterey, CA, Apr. 2007.
- [21] V. DOLEJŠÍ AND M. FEISTAUER, *A semi-implicit discontinuous Galerkin finite element method for the numerical solution of inviscid compressible flow*, J. Comp. Phys., 198 (2004), pp. 727–746.
- [22] D.R. DURRAN, *Numerical methods for wave equations in geophysical fluid dynamics*, Springer-Verlag, New York, 1999.
- [23] D.R. DURRAN AND J.B. KLEMP, *A compressible model for the simulation of moist mountain waves*, Mon. Wea. Rev., 111 (1983), pp. 2341–2361.
- [24] A. GASSMANN, *An improved two-time-level split-explicit integration scheme for non-hydrostatic compressible models*, Meteorol. Atmos. Phys., 88 (2005), pp. 23–38.
- [25] A. GASSMANN AND H.J. HERZOG, *A consistent time-split numerical scheme applied to the nonhydrostatic compressible equations.*, Mon. Wea. Rev., 135 (2007), pp. 20–36.
- [26] F.X. GIRALDO, *Semi-implicit time-integrators for a scalable spectral element atmospheric model*, Q. J. R. Meteorol. Soc., 131 (2005), pp. 2431–2454.
- [27] —, *High-order triangle-based discontinuous Galerkin methods for hyperbolic equations on a rotating sphere*, J. Comp. Phys., 214 (2006), pp. 447–465.
- [28] F.X. GIRALDO, J.S. HESTHAVEN, AND T. WARBURTON, *Nodal high-order discontinuous Galerkin methods for the spherical shallow water equations*, J. Comp. Phys., 181 (2002), pp. 499–525.
- [29] F.X. GIRALDO AND M. RESTELLI, *A study of spectral element and discontinuous Galerkin methods for mesoscale atmospheric modeling: equation sets and test cases*, J. Comp. Phys., submitted (2007).
- [30] F.X. GIRALDO AND T. WARBURTON, *A high-order triangular discontinuous Galerkin oceanic shallow water model*, Int. J. Numer. Meth. Fl., in press (2007).
- [31] G.E. KARNIADAKIS, M. ISRAELI, AND S.A. ORSZAG, *High-order splitting methods for the incompressible Navier–Stokes equations*, J. Comp. Phys., 97 (1991), pp. 414–443.
- [32] J.B. KLEMP AND D.K. LILLY, *Numerical simulation of hydrostatic mountain waves*, J. Atmos. Sci., 35 (1978), pp. 78–107.
- [33] J.B. KLEMP, W.C. SKAMAROCK, AND J. DUDHIA, *Conservative split-explicit time integration methods for the compressible nonhydrostatic equations*, Mon. Wea. Rev., (to appear).
- [34] M. KWIZAK AND A.J. ROBERT, *A semi-implicit scheme for grid point atmospheric models of the primitive equations*, Mon. Wea. Rev., 99 (1971), pp. 32–36.
- [35] R.D. NAIR, S.J. THOMAS, AND R.D. LOFT, *A discontinuous Galerkin global shallow water*



- model*, Mon. Wea. Rev., 133 (2005), pp. 876–888.
- [36] J.P. PINTY, R. BENOIT, E. RICHARD, AND R. LAPRISE, *Simple tests of a semi-implicit semi-Lagrangian model on 2D mountain wave problems*, Mon. Wea. Rev., 123 (1995), pp. 3042–3058.
  - [37] M. RESTELLI, *Semi-Lagrangian and semi-implicit discontinuous Galerkin methods for atmospheric modeling applications*, PhD thesis, Politecnico di Milano, 2007.
  - [38] M. RESTELLI, L. BONAVENTURA, AND R. SACCO, *A semi-Lagrangian discontinuous Galerkin method for scalar advection by incompressible flows*, J. Comp. Phys., 216 (2006), pp. 195–215.
  - [39] H. RITCHIE, C. TEMPERTON, A. SIMMONS, M. HORTAL, T. DAVIES, D. DENT, AND M. HAMRUD, *Implementation of the semi-Lagrangian method in a high-resolution version of the ECMWF forecast model*, Mon. Wea. Rev., 123 (1995), pp. 489–514.
  - [40] A. ROBERT, *Bubble convection experiments with a semi-implicit formulation of the Euler equations*, J. Atmos. Sci., 50 (1993), pp. 1865–1873.
  - [41] V.V. RUSANOV, *Calculation of interaction of non-steady shock waves with obstacles*, USSR Comp. Math. and Math. Phys., 1 (1961.), pp. 267–279.
  - [42] C. SCHÄR, D. LEUENBERGER, O. FUHRER, D. LÜTHI, AND C. GIRARD, *A new terrain-following vertical coordinate formulation for atmospheric prediction models*, Mon. Wea. Rev., 130 (2002), pp. 2459–2480.
  - [43] D. SCHWANENBERG AND J. KÖNGETER, *A discontinuous Galerkin method for the shallow water equations with source terms*, in *Discontinuous Galerkin methods*, Springer, 2000, pp. 419–424.
  - [44] A.J. SIMMONS, B.J. HOSKINS, AND D.M. BURRIDGE, *Stability of the semi-implicit method of time integration*, Mon. Wea. Rev., 106 (1978), pp. 405–412.
  - [45] W.C. SKAMAROCK AND J.B. KLEMP, *Efficiency and accuracy of the Klemp–Wilhelmson time-splitting technique*, Mon. Wea. Rev., 122 (1994), pp. 2623–2630.
  - [46] R.B. SMITH, *The influence of mountains on the atmosphere*, Adv. Geophys., 221 (1979), pp. 87–
  - [47] J.M. STRAKA, R.B. WILHELMSON, L.J. WICKER, J.R. ANDERSON, AND K.K. DROEGEMEIER, *Numerical solutions of a non-linear density current: A benchmark solution and comparisons*, Int. J. Numer. Meth. Fl., 17 (1993), pp. 1–22.
  - [48] M. TANGUAY, A. ROBERT, AND R. LAPRISE, *A semi-implicit semi-Lagrangian fully compressible regional forecast model*, Mon. Wea. Rev., 118 (1990), pp. 1970–1980.
  - [49] M.C. TAPP AND P.W. WHITE, *A non-hydrostatic mesoscale model*, Q. J. R. Meteorol. Soc., 102 (1976), pp. 277–296.
  - [50] E.F. TORO, *Riemann solvers and numerical methods for fluid dynamics*, Springer–Verlag, Berlin, Heidelberg, 1997.